Industrial Crops & Products 223 (2025) 120125

Contents lists available at ScienceDirect

Industrial Crops & Products

journal homepage: www.elsevier.com/locate/indcrop

Purification of bioactive compounds from rosemary by-products for innovative solutions in food industry

Imane Ziani [a,b,*], Hamza Bouakline [a], Mohammed Merzouki [c], Marie-Laure Fauconnier [d], Farooq Sher [e,**], Nour Eddine Bentouhami [f], Abdeslam Asehraou [f], Ali El Bachiri [a]

[a] Physical Chemistry of Natural Substances and Process Research Team, Laboratory of Applied Chemistry and Environment, Faculty of Sciences, Chemistry Department, Mohammed First University, Oujda 60000, Morocco
[b] International Society of Engineering Science and Technology, United Kingdom
[c] Laboratory of Applied Chemistry and Environment, Faculty of Sciences, Chemistry Department, Mohammed First University, Oujda 60000, Morocco
[d] Laboratory of Chemistry of Natural Molecules, Gembloux Agro-Bio Tech, University of Liège, Liège, Belgium
[e] Department of Engineering, School of Science and Technology, Nottingham Trent University, Nottingham NG11 8NS, United Kingdom
[f] Laboratory of Bio-Resources, Biotechnology, Ethno-Pharmacology and Health, Faculty of Sciences, Biology Department, Mohammed First University, Oujda 60000, Morocco

ARTICLE INFO

Keywords:
By-products valorization
Flash chromatography
^{2}D NMR techniques
Phenolic compounds
Multifunctional bioactive agents and molecular docking

ABSTRACT

Maximizing the value of agricultural by-products is critical for advancing sustainable development and minimizing waste. This study delves into the solid by-products of *Rosmarinus tournefortii* de Noé, focusing on their fractionation and purification to unveil valuable bioactive compounds. Using flash chromatography, nine distinct fractions (F1 to F9) were successfully isolated. Cutting-edge analytical techniques including FTIR, UHPLC-MS/MS, and ^{2}D NMR (HSQC, HMBC and COSY) confirmed the presence of novel labdane diterpenoids (PF1), 24-nor-ursane triterpenoids (PF5), and ent-kaurane diterpenoids (PF6). Furthermore, HPLC-DAD profiling revealed rosmadial (79.43 % in F4) and luteolin (70.14 % in F7) as the dominant phenolic compounds. Notably, the crude extract demonstrated remarkable antioxidant activity, with an IC50 of 0.04±0.23 mg/mL. Fractions F7 and F8 also exhibited strong antioxidant potential, with IC50 values of 0.35±0.07 mg/mL and 0.36±0.02 mg/mL, respectively. Purified fractions PF7 and F8, enriched with luteolin and 3-hydroxyflavone, proved highly effective for pigmentation control, with PF7 showing an IC50 of 0.045±0.007 mg/mL. In addition, antimicrobial assays revealed that the 24-nor-ursane triterpenoid and fraction F6, containing ent-kaurane and carnosol, displayed potent inhibitory effects against *Rhodotorula glutinis* (24.1 mm). Molecular docking studies further highlighted PF5 as a potent inhibitor of alpha-amylase (-5.856 kcal/mol) and tyrosinase (-4.385 kcal/mol), while PF1 surpassed acarbose in alpha-glucosidase inhibition with a binding energy of −5.898 kcal/mol. Collectively, these findings highlight the immense potential of *R. tournefortii* by-products as a rich source of bioactive compounds for health and skincare, offering promising, sustainable solutions for the pharmaceutical, cosmetic and food preservation industries.

1. Introduction

The linear model remains dominant in the current global market, characterized by a "produce, use and dispose" approach. Within this system, 76 % of waste goes to landfills or incinerators, while only 12 % is recycled (Mir-Cerdà et al., 2023). The circular economy framework opposes this model by minimizing material usage and waste generation through optimized recycling and using wastes as inputs for new material creation. This shift is essential for transforming waste into useful resources and achieving sustainability (Freitas et al., 2021). Studies on food products' chemical and functional features highlight the vast variety of bioactive compounds present in non-edible parts. Extracted compounds can offer significant value across several sectors, including functional food, nutraceutical, pharmaceutical, and cosmeceutical

* Corresponding author at: Physical Chemistry of Natural Substances and Process Research Team, Laboratory of Applied Chemistry and Environment, Faculty of Sciences, Chemistry Department, Mohammed First University, Oujda 60000, Morocco.
** Corresponding author.
E-mail addresses: imane.ziani95@outlook.com (I. Ziani), Farooq.Sher@ntu.ac.uk (F. Sher).

https://doi.org/10.1016/j.indcrop.2024.120125
Received 20 September 2024; Received in revised form 14 November 2024; Accepted 19 November 2024
Available online 26 November 2024

industries (Mohammadnezhad et al., 2023). Recovering bioactive compounds from food-origin waste has become a central focus of food science, providing a cost-effective and eco-friendly approach for the food industry (Capanoglu et al., 2022).

Recent work has highlighted the potential of industrial waste as a source of valuable compound isolation. For instance, Shen et al. (2022) developed a two-dimensional chromatography system coupled with a macroporous adsorption resin, achieving purities above 99.0 % of high-purity bioflavonoids from *Ginkgo biloba* exocarp wastes. Similarly, Bermúdez-Oria et al. (2024) isolated trans and cis-p-coumaroyl-secologanoside from olive oil waste at purities ranging from 80 % to 85 %, along with enhanced antioxidant activity. These studies are extremely important for the efficient sequential isolation of industrially valuable compounds from wastes, creating new opportunities for the development of bioactive agents within the scope of green pharmaceutical chemistry.

Building on these concepts, the genus *Rosmarinus* L., part of the Lamiaceae family, includes three Mediterranean-native species: *Rosmarinus tournefortii* de Noé, *Rosmarinus officinalis* L., and *Rosmarinus tomentosus* (Najar et al., 2020). *R. tournefortii* (also known as *Rosmarinus eriocalyx* Jord. & Fourr. or *Salvia jordanii* J.B.Walker) is an aromatic evergreen shrub native to the Mediterranean, particularly abundant in North Africa, including Algeria, Morocco, and parts of Spain. Closely related to *R. officinalis*, it is distinguished by its smaller, densely hairy leaves (5–15 mm long and less than 2 mm wide) and double glandular hairs on the flower stems and calyx (Bendif et al., 2017a). Typically found in rocky, mountainous areas, *R. tournefortii* grows prostrate, generally under 25 cm in height but occasionally reaching up to 1 m. *R. tournefortii* has long been valued for its rich phenolic content, which provides potent anti-inflammatory effects and supports various medicinal applications (Nunziata et al., 2019). It is commonly used as a digestive aid to relieve abdominal pain, bloating, diarrhea, and gas. Additionally, it supports respiratory health by treating coughs and asthma, acts as a febrifuge to reduce fevers, and helps manage low blood pressure (Bendif et al., 2018). Beyond its medicinal applications, *R. tournefortii* exhibits strong antioxidant and antimicrobial properties, making it valuable in food preservation, cosmetics, and agriculture (Bensouici et al., 2020). Its ability to combat oxidative stress and inhibit microbial growth highlights its potential as a natural preservative and pesticide, with wide-ranging applications across various industries.

Despite the extensive study of *R. tournefortii* extracts, the by-products from plant-based industries remain underutilized. Our group has previously published studies focusing on optimizing the extraction of bioactive compounds from *R. tournefortii* solid by-products, identifying the best ethanol/water solvent mixtures to maximize phenolic content and biological activity (Ziani et al., 2023). Furthermore, *R. tournefortii* by-products, especially those from wastewater, have demonstrated superior antioxidant capacity and significant inhibition of pancreatic α-amylase, highlighting their potential for diabetes management and environmental sustainability (Ziani et al., 2024a). Additionally, nanotechnology studies have shown that green-synthesized silver nanoparticles (AgNPs) derived from *R. tournefortii* by-products improved biodegradable composites, emphasizing the plant's potential for sustainable development and advanced material science applications (Ziani et al., 2024b). While extraction and valorization of *R. tournefortii* by-products have been explored, studies on the purification of specific bioactive molecules remain absent. In contrast, Chen et al. (2022) identified new labdane and isopimarane diterpenoids exhibiting relevant neuroprotective effects against oxidative damage in SH-SY5Y cells from *R. officinalis* solid wastes after essential oil extraction. This is the only study to date focusing on the purification of rosemary by-products, highlighting the need for similar research on *R. tournefortii* and marking it as a promising area for future exploration.

For this purpose, the present study investigates the bioactive potential of solid by-products of *R. tournefortii* by identifying and characterizing novel complex compounds using thin-layer chromatography (TLC), high-performance liquid chromatography (HPLC) and UHPLC-MS/MS. New compounds, including labdane diterpenoids, nor-ursane triterpenoids, and ent-kaurene diterpenoids, are further analyzed using FTIR and ^{1}D and ^{2}D NMR techniques (including HSQC, HMBC and COSY). The bioactivities of these compounds, including antioxidant, tyrosinase inhibition and antimicrobial activities, are evaluated for their potential applications in pharmaceuticals, cosmetics and food preservation. Furthermore, molecular docking studies on purified compounds assess their binding affinities and mechanisms of action against alpha-amylase, alpha-glucosidase and tyrosinase. These docking studies provide insights into the compounds' efficacy and enhance understanding of their bioactivity. Such studies are essential for understanding the interaction between the compounds and target enzymes, offering insights into their efficacy and predicting their bioactivity. Additionally, the impact of purification and fractionation on bioactivity is investigated to determine whether these processes enhance the effectiveness of the compounds. The study's significance lies in its potential to offer sustainable solutions for agricultural waste recovery and advance the use of bioactive compounds in various industries.

2. Materials and methods

2.1. Plant material, extraction, fractionation and purification

Fresh leaves from the wild plant *Rosmarinus tournefortii* de Noé were harvested during the flowering stage on 15 March 2022, from the Megrez forest in the Oriental region of Morocco (Ziani et al., 2024b, 2023). The plant was authenticated by botanist Elachouri Mostafa from Mohammed First University, Oujda, and the specimen was recorded in the university's herbarium under the reference number HUMPOM-812. The fresh leaves were air-dried in the shade at room temperature for 10 days. Once dried, approximately 100 kg of leaves were distilled on a pilot scale for 3 hours to extract the essential oil. The solid by-product resulting from this distillation process was then powdered and air-dried for an additional 15 days. After drying, the pulverized solid by-product was extracted with 250 mL of methanol in a Soxhlet apparatus for 8 hours. The extract obtained was concentrated and fractionated on a 40–60 μm silica gel column, eluted with solvents of increasing polarity, to give 9 fractions (Fig. 1(A)). More specifically, the first fraction, F1, was obtained with 100 % hexane. For the second, third and fourth fractions, a 50–80 % hexane gradient in ethyl acetate was used. The fifth fraction, F5, was eluted with 100 % ethyl acetate. The sixth and seventh fractions were eluted with 80 % and 0 % ethyl acetate in methanol, respectively. The last two fractions were obtained using an eluent of 0.1 % formic acid in water. During fractionation, pressure was manually applied by adjusting the valve to regulate the flow through the flash column. To further analyse the compounds present in the fractions, thin-layer chromatography was performed in 0.25 mm, 40–60 μm, 230–400 mesh. Four fractions were considered for purification, namely F1, F5, F6 and F7. The first fraction F1 was purified by several ethanol washes. Similarly, fractions F6 and F7 were purified using ethyl acetate. Fraction F5 was further purified by recrystallization in 50 % ethanol in methanol.

2.2. Spectroscopic characterisation

Compounds isolated from the by-product fractionation of *R. tournefortii* were characterized using various analytical techniques. The first approach involved Attenuated Total Reflectance-Fourier Transform Infrared analysis, conducted with a Jasco 4700-FTIR spectrometer from Shimadzu, Japan. This analysis aimed to compare the properties of dehydrated plant material with those of the isolated compounds and to determine the primary functional groups present (El Guerraf et al., 2023). ATR-FTIR spectra were recorded over a wavelength range of 500–4000 cm^{-1}. Nuclear magnetic resonance spectroscopy was also performed to verify and characterize the molecular

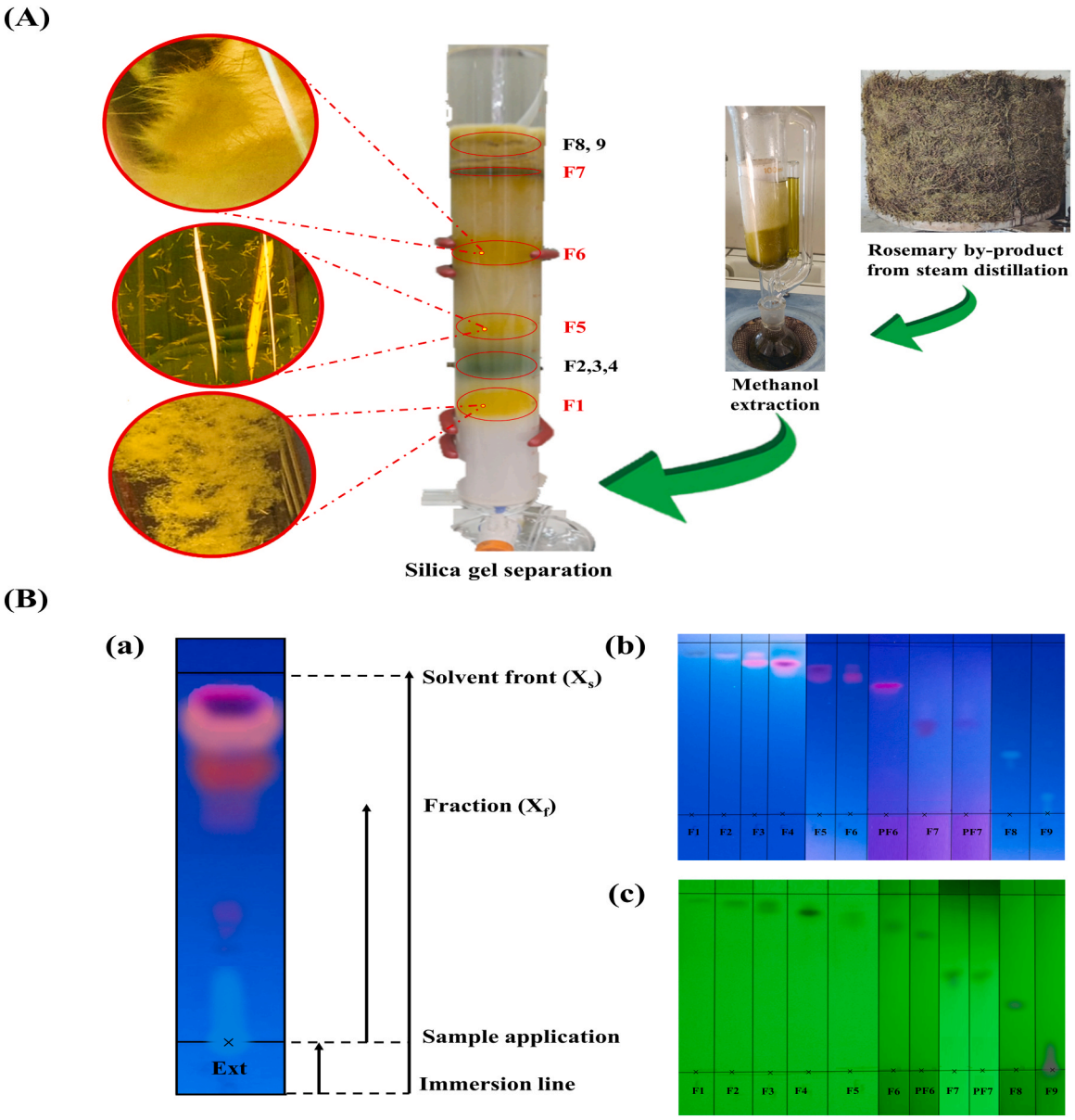

Fig. 1. (A) Extraction, fractionation, and selected fraction (F1, F5 and F6) for the purification process of *R. tournefortii* solid by-product. (B) Thin layer chromatographic analysis of the methanolic extract from the solid by-product of *R. tournefortii*.

structure of these compounds. In addition to ^{1}D NMR spectra, three key ^{2}D NMR methods were employed: Heteronuclear Single Quantum Coherence Heteronuclear (HSQC), Multiple Bond Correlation (HMBC) and Homonuclear Correlation Spectroscopy (COSY) (Elyashberg, 2015). NMR spectra were obtained using a Bruker Avance 700 MHz spectrometer for 1H, HMBC, HSQC and COSY experiments. Chemical shifts (δ) were referenced relative to tetramethylsilane (TMS) and residual proton solvent resonances: DMSO at 2.50 ppm for 1H and 39.5 ppm for HMBC and HSQC; Ethanol at 1.06, 3.44, and 4.35 ppm for 1H, and 18.51 and 56.07 ppm for HMBC and HSQC; and Methanol at 3.17 and 4.10 ppm for 1H, and 48.59 ppm for HMBC and HSQC NMR (Ruan et al., 2022).

2.3. Chemical profile of separated compounds

HPLC analysis was performed based on the method described by Liu et al. (Liu et al., 2011). The analytical column used was a reverse phase Zorbax SB-C18 column (4.6 mm × 250 mm, 5 µm) at ambient temperature. A volume of 10 µL of each sample was injected into a Hewlett-Packard system from Germany, equipped with a quaternary pump and a photodiode array UV−vis detector. Acetonitrile (A) and water (B) were used as the mobile phase, both of which were acidified with 0.1 % formic acid. The gradient was described as follows: 0 min, 40 % A; 2 min, 50 % A; 10 min, 50 % A; 15 min, 70 % A; 25 min, 70 % A; 32 min, 40 % A. The flow rate stood at 0.5 mL/min, with detection wavelengths configured at 280 and 330 nm. By examining retention periods and spectra alongside commercially available reference compounds, the phenolic components were pinpointed. Additionally, the first three fractions and the isolated compounds were analyzed via direct injection in negative mode using UHPLC-MS/MS (a UHPLC Agilent 1290 Infinity II LC combined with an Agilent 6470 Triple Quad LC-MS/MS mass detector with MassHunter ChemStation) to determine the mass spectra within a scan range of 50–1100 *m/z*.

2.4. DPPH• radical scavenging capacity

The ability of *R. tournefortii* by-product fractions and their isolated compounds to scavenge DPPH• free radicals was assessed using the

technique published by Mahnashi et al. (2021). The procedure relied on the creation of the nonradical DPPH-H form, which occurs when the free radical DPPH is stabilized by a hydrogen-donating antioxidant (Mollica et al., 2019). Briefly, 500 µL of both the crude extract and its purified fractions were combined with 2500 µL of DPPH radical solution (4 mg/100 mL). The resulting solution was incubated in dark conditions for 60 min at ambient temperature. A UV-Vis spectrophotometer was applied to quantify the absorbance at 517 nm. DPPH-radical inhibition (%) was calculated based on the following equation Eq. (1) (Bouakline et al., 2024).

$$DPPH\ Inhibition(\%) = \frac{A0 - AC}{A0} \times 100 \quad (1)$$

Where $A0$ is the absorbance value of the negative control and AC is the absorbance value of the tested sample. The DPPH radical-scavenging activity was quantified as the IC50 value, which represents the concentration required to inhibit 50 % of the free radicals. This value is determined graphically by plotting the inhibition percentage (I%) against the concentration (C) and extrapolating the concentration corresponding to 50 % inhibition from the curve along the x-axis.

2.5. Tyrosinase inhibition

Inhibition of tyrosinase was assessed using the tyrosinase enzyme as described by Peng et al. (2021) with modest modification. The enzyme solution (625 U/mL) was prepared by mixing 0.95 mg of the commercial enzyme (6540 U) in 10 mL of phosphate buffer (0.05 M, pH 6.5). The solution was divided into 1 mL portions and frozen at −22°C until use. The aliquots were frozen only once. During handling, the enzyme solution was kept in an ice bath and prevented from reaching room temperature to avoid enzyme hydrolysis and loss of activity (Stefanucci et al., 2020). Briefly, 100 µL of samples (dissolved in phosphate buffer) at different concentrations (0.01–1 mg/mL) were mixed with 50 µL of tyrosinase (625 U/mL), then 250 µL of phosphate buffer (0.05 M, pH 6.5) was added. After a 15-minute pre-incubation at room temperature, 400 µL of L-Dopa (1 mM) as substrate was added to the mixture to start the enzymatic reaction. The kinetics of inhibition for tyrosinase were measured at 15-sec intervals for 5 min at 475 nm using the UV–VIS spectrophotometer, Shimadzu UV 1650-PC. The tyrosinase inhibition rate was determined according to Eq. (2) (Peng et al., 2021). Where A0 corresponds to the phosphate buffer, representing the absorbance of the negative control, and AC corresponds to the samples tested. Linear regression analysis was applied to calculate the concentration of the crude extract and its fractions (IC50) needed to inhibit 50 % of tyrosinase.

$$Tyrosinase\ Inhibition(\%) = \frac{(A0 - AC)}{A0} \times 100 \quad (2)$$

2.6. Bacterial strains and growth conditions

The antimicrobial activity of the crude *R. tournefortii* solid by-products, fractions and isolated compounds against eight common food-borne pathogens. These pathogens included two Gram-positive strains: *L. innocua* (ATCC 33090) and *S. aureus* (ATCC 25923); two Gram-negative strains: *E. coli* (ATCC 25922) and *P. aeruginosa* (ATCC 27853); two molds: *Geotrichum sp.* (ATCC 34614) and *Aspergillus niger* (ATCC 16404); and two yeasts: *Penicillium* (ATCC 7861) and *Rhodotorula glutinis* (ATCC 15125). All bacterial and fungal strains were obtained from the American Type Culture Collection (ATCC). The antimicrobial activity was tested using the agar diffusion method. Strains of Gram-negative and Gram-positive bacteria, yeasts, and molds were diluted and adjusted to 0.5 McFarland, corresponding to 10^6 CFU/mL for bacteria and yeasts, and 10^6 spores/mL for molds. Fresh cultures were diluted in Mueller-Hinton broth in the case of bacteria, yeasts, and molds, and in sterile physiological water, they were used for both before inoculation on the surface of the Petri dish. The solid-state diffusion assay, as described by Zamuz et al. (2021), was applied. Mueller-Hinton agar (MHA), seeded with the bacterium or fungus to be tested is perforated to create wells (6 mm), which are then filled with a 10 µL volume of sample (2 mg/mL). Agar plates were incubated for bacterial growth for 18 hours at 37 °C and for fungal growth for 48 hours at 25°C (Bhattacharjee et al., 2022). The diameter of the inhibition zone in the agar gel was used to assess the antimicrobial activity of the crude *R. tournefortii* by-product extract and its fractions. Each test was performed three times. Positive controls against fungi and bacteria were cycloheximide and gentamicin, respectively.

2.7. Computational simulation and molecular interaction study

2.7.1. Ligands preparation

The three-purified compounds, PF1, PF5 and PF6, were molecularly modelled using Maestro version 13.8 from Schrodinger LLC, New York, NY, USA (Zhang et al., 2021). To compare the result of the experiment, Acarbose and kojic acid were employed as positive control standards. The correct bond order was used in the preparation of the structure with the help of LigPrep package from the Schrodinger software system. All compounds were then translated to SDF format by using Maestro and minimized with OPLS 2005 force field using the default parameters for energy minimization (Vant et al., 2020).

2.7.2. Molecular docking and protein synthesis

Molecular docking investigations were conducted using X-ray crystal structures obtained from the Protein Data Bank. The structures analyzed included "Human Pancreatic Alpha-Amylase Bound to Acarbose" (PDB ID 1B2Y, 3.20 Å resolution), "Human Lysosomal Acid-Alpha-Glucosidase Bound to Acarbose" (PDB ID 5NN8, 2.45 Å resolution), and "Tyrosinase (PDB ID 3NQ1, 2.30 Å resolution) from Bacillus megaterium Bound to Kojic Acid" (Siddique et al., 2022). The preparation of these protein structures was done using the Protein Preparation Wizard in Maestro 13.8 by Schrodinger, LLC, based in New York, NY, USA. This method involved removing ligands and water molecules before combining non-polar hydrogens. The docking target was determined to be the active site. A central grid box including all ligand atoms was constructed, with 20 points allotted to each of the three axes (x, y, and z) to ensure the optimal docking environment. Using default settings and an RMSD restriction of 0.3 Å, energy reduction was carried out (Sharma et al., 2021). Binding predictions were produced by selecting relevant postures with the standard precision glide score, and docking scores were presented as binding affinities in kcal/mol. Protein structures were further reduced using the OPLS_2005 force field (Sindhu and Srinivasan, 2015), and the interactions between proteins and ligands were visualized with the Ligand Interaction Diagram package.

2.8. Statistical analysis

The results were processed using descriptive statistical analysis, analysis of variance (ANOVA), and regression analysis with SPSS for Windows, version 20. One-way ANOVA was performed to assess significant differences between treatment groups. Tukey's Honest Significant Difference (HSD) post hoc test was performed at a significance level of 5 % ($p < 0.05$) to make pairwise comparisons. All experiments were performed in triplicate and results are expressed as means and standard deviations. Statistical analyses assessed significant differences between treatment groups; groups sharing the same letter were not significantly different from each other ($p \geq 0.05$).

3. Results and discussion

3.1. Thin-layer chromatography revelation

After extraction and fractionation using a flash column, TLC was

performed to identify the molecules present in the methanolic extract of *R. tournefortii* solid by-products. The concentrated methanolic extract was fractionated using solvents of varying polarity on a silica gel flash column, resulting in nine fractions labelled from F1 to F9, as shown in Fig. 1**(B)**. The Rf values of each fraction obtained by TLC on silica gel plates were as follows: Rf1 = 0.95, Rf2 = 0.95/0.91, Rf3 = 0.91/0.88, Rf4 = 0.88/0.84, Rf5 = 0.84/0.80, Rf6= 0.80, Rf7 = 0.53/0.49, Rf8 = 0.35/0.31 and Rf9 = 0.08. Certain eluates, such as fractions Rf1 and Rf6, displayed a single spot on the TLC plate.

In contrast, other fractions produced two distinct but related spots, indicating the presence of two different compound families. In TLC, the Rf value refers to the distance a compound travels relative to the solvent front. Compounds with lower Rf values are more strongly retained by the silica gel stationary phase and therefore travel shorter distances, indicating higher polarity (Striegel, 2020). In contrast, compounds with higher Rf values travel further down the chromatogram, indicating lower polarity. Since Rf values can be used to deduce the relative polarity of compounds, lower Rf values, such as Rf9, generally indicate high polarity. The Rf values provide a representation of the polarity of the compounds. The value measured for each compound gives an idea of the chemical nature of the fraction, corresponding to the rosemary by-product fractions. Fractions with closely spaced spots, such as Rf2, Rf3, Rf4, Rf5, Rf7 and Rf8, are made up of compounds with similar polarities, which explains the difficulty in separating compounds with very similar chemical properties.

Compared to our results, the existing literature supports these observed polarity trends and provides insight into the likely identities of compounds in our fractions, though some differences appear. For example, Morlock et al. (2021) identified rosmarinic acid with an Rf value of 0.90 and carnosol with an Rf value of 0.73 using high-performance thin-layer chromatography (HPTLC). Typically, carnosol, which is less polar than rosmarinic acid, should have a higher Rf value, meaning it should migrate further. However, the opposite is observed, probably due to differences in TLC conditions, such as solvent systems or modifications to the stationary phase, which can affect the migration and retention of compounds. Other studies, such as those by Agatonovic-Kustrin et al. (Agatonovic-Kustrin et al., 2021) identified rosmarinic acid at an Rf of 0.10, caffeic acid at Rf 0.37 and carnosic acid at Rf 0.53, corresponding to our lowest Rf fractions, suggesting similar polarity. Similarly, Sharma et al. (2020) of caffeic acid (Rf = 0.40) and ursolic acid (Rf = 0.82) corresponded closely to our average fractions, confirming our observations on relative polarity. Additionally, Su et al. (2020) identified rosmarinic acid at an Rf of around 0.486 in *R. officinallis*, corroborating the behavior of polar compounds in our study. Collectively, these comparative studies validate our use of TLC and flash column fractionation to establish the polarity profile of rosemary bioactive compounds, demonstrating a general agreement between studies regarding compound types and their Rf behaviour.

3.2. Yield analysis of methanolic extract fractions

In the extraction of *R. tournefortii* by-product, the yield of the methanolic extract was calculated relative to the initial mass of the powdered *R. tournefortii* by-product used in the Soxhlet apparatus. Methanol was selected for its high polarity, which allows the effective dissolution of various compounds, and its low boiling point, enabling efficient separation and recovery with minimal energy input. These properties make methanol both efficient and cost-effective for high-purity extraction (Zhang et al., 2020). The resulting methanolic extract had a deep green colour and a yield of 34.5±0.9 %. Yield analysis of the methanolic extract fractions revealed significant variability, as shown in Table 1, which presents the results of fractionation using flash column chromatography with various eluting solvent systems. A total of 9 fractions were identified based on their thin-layer chromatography (TLC) profiles, and yields were calculated relative to the initial crude extract mass. Fraction F1 showed the highest yield at 27.58 ±0.67 %, likely due to a high concentration of specific compounds, while fraction F2 had a much lower yield of 3.08±0.72 %, suggesting fewer or lower-concentration compounds. Statistical analysis confirmed significant differences among fractions ($P < 0.05$), underscoring this distribution variability. Moderate yields observed in fractions F3 through F6 (ranging from 5.75±0.98 % to 7.62±0.2 %) imply the presence of compounds in moderately concentrated forms, whereas F7, with a yield of 9.33±1.02 %, and final fractions F8 and F9, yielding 15.09±0.54 % and 16.4±0.93 %, respectively, support a concentration effect rather than compound diversity.

Table 1
The recovery yield of *R. tournefortii* extract fractions relative to the initial mass of the crude extract.

Samples	Yield (% w/w of crude extract)
F1	27.58±0.67[a]
F2	3.08±0.72[b]
F3	5.75±0.98[c]
F4	7.01±0.32[c]
F5	6.76±1.13[c]
F6	7.62±0.2[c]
F7	9.33±1.02[d]
F8	15.09±0.54[e]
F9	16.4±0.93[e]

*__Note:__ Distinct superscript letters within each column signify that the means differ significantly ($p < 0.05$). Values are expressed as Mean ± Standard Deviation ($n = 3$).

Comparing these findings with the literature reveals consistent trends in the fractionation process. For example, Kabubii et al. (2024) reported the fractionation of *R. officinalis* extract into 21 fractions with yields spanning a wide range, where fraction F12 had the highest yield at 30.43 g, followed by F13 at 22.45 g, while others, such as F2, yielded as little as 0.12 g. This pattern of variability aligns with our findings, where yields ranged from 3.08±0.72 % in F2 to 27.58±0.67 % in F1, indicating that certain fractions concentrate high-yield compounds. Chen et al. (2022) also documented yield distribution from R. officinalis residues post-essential oil extraction, which initially produced four primary fractions. Fraction Fr.3, weighing approximately 500 g, was further fractionated, resulting in subfractions with distinct yields, such as Fr.3–4–3 (25 g). Certain fractions demonstrated notably higher yields in all studies, suggesting that fractionation processes selectively concentrate particular compounds. These findings underscore the variable nature of rosemary fractionation, likely due to the efficiency of specific solvents and column chromatography conditions in isolating distinct compounds. This research primarily focused on the fractions of solid by-products of *R. tournefortii* in the eastern region of Morocco. The absence of separated fractions from these by-products suggests that further investigation is warranted in future studies.

3.3. Vibrational characterization

The FTIR spectra of the samples, comprising the extract and the purified fractions PF1, PF5 and PF6, are shown in Fig. 2, providing essential information about their chemical structure. For example, the spectrum of PF1 reveals the presence of aliphatic hydrocarbons, as indicated by the strong C-H stretching bands at around 2920 cm^{-1} and 2850 cm^{-1}. The carbonyl (C═O) stretching peak at 1595 cm^{-1} suggests the presence of carbonyl-containing groups, such as esters or ketones. In addition, the strong C-O stretching bands observed at ~1240 cm^{-1} and 1050 cm^{-1} indicate the presence of other compounds. The spectrum of the extract shows a broad O-H stretch around 3350 cm^{-1}, characteristic of hydroxyl groups, probably carboxylic acids. It also shows C-H stretching bands around 2920 cm^{-1} and 2850 cm^{-1}, as well as carbonyl stretching around 1593 cm^{-1} and 1695 cm^{-1}. The presence of a C═C stretch at ~1610 cm^{-1} and 1510 cm^{-1}, combined with a larger C-O

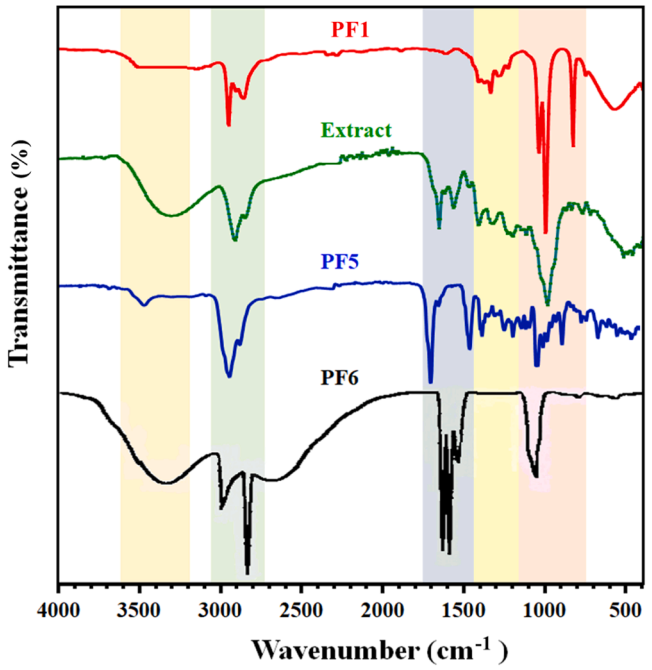

Fig. 2. ATR-FTIR analysis of purified compounds from *R. tournefortii* solid by-products obtained through column fractionation.

stretch at ~1050 cm^{-1}, suggests a higher concentration or different configuration of ethers or esters compared to PF1. These variations highlight significant differences in composition, which may result from the presence of additional functional groups or molecular interactions. In the PF5 spectrum, a broad O-H stretch near 3490 cm^{-1} suggests the presence of carboxylic acid hydroxyl groups. The C-H and C═O stretching regions are similar to those observed in the extract, indicating the presence of similar functionalities. The spectrum of PF6 closely resembles that of PF5, with only minor changes in peak position and intensity. A broad O-H stretch around 3300 cm^{-1} and strong C═O stretches at 1595 cm^{-1} and 1635 cm^{-1} confirm the presence of hydroxyl and carbonyl groups, respectively. Remarkable C-O stretching peaks near 1080 cm^{-1}, in particular the pronounced band around 1000–1050 cm^{-1}, suggest significant ester or ether functionalities. These slight shifts may reflect differences in molecular structure or sample preparation.

Comparing our results with the existing literature, labdane diterpenoids generally exhibit a strong C═O stretch band around 1720 cm^{-1}, an O-H stretch near 3400 cm^{-1}, and a C-O stretch band between 1000 and 1050 cm^{-1} (Chen et al., 2022). In PF1, a similar C-O stretch is observed, consistent with the ether or ester functionalities expected in labdane structures. However, the C═O stretch in PF1 appears at a slightly lower frequency, suggesting possible structural differences in the carbonyl environment or unique molecular interactions that distinguish it from standard labdane profiles. In contrast, norursane triterpenoids show a C═O stretch at 1689 cm^{-1}, an O-H stretch at 3432 cm^{-1}, and a C-O stretch at around 1238 cm^{-1} (Jang et al., 2005). In addition, Zhong et al. (2022) reported typical aliphatic C-H stretches between 2920 and 2860 cm^{-1} and aromatic ring vibrations around 1450 cm^{-1} reflect a diverse functional environment. Compared to these values, the frequency of C═O stretching in PF5 is observed at slightly lower values than in the literature, suggesting potential variations in binding environments or functional group interactions within PF5. Ent-kaurene diterpenoids generally exhibit an O-H stretching around 3400 cm^{-1}, a C═O stretching around 1700 cm^{-1} and a C-O stretching between 1000 and 1050 cm^{-1} (Márquez et al., 2023). In addition, FTIR spectra of ent-kaurane diterpenoids also include aliphatic C-H stretches in the range 2950–2850 cm^{-1} and, occasionally, a broad O-H stretch suggesting prevalent hydroxy groups (Zhang et al., 2017). In PF6, similar absorption bands are observed, although minor shifts in the O-H and C═O stretching frequencies may reflect subtle differences in hydroxy or carbonyl configurations, slightly distinguishing PF6 from standard ent-kaurene profiles.

Further, the ATR-FTIR spectrum of rosemary extract also reveals similar peaks, with an O-H stretch around 3300–3400 cm^{-1}, a C═O stretch around 1700 cm^{-1}, and a C-O stretch between 1000 and 1100 cm^{-1}, indicating the presence of phenolic, carbonyl and ether groups, respectively (Tsiaka et al., 2023). This comparison suggests that the functional groups present in the isolated compounds are common to all samples, making it difficult to accurately identify the diterpenoid family based on FTIR data alone. The overlapping absorption bands for O-H, C═O and C-O stretching, typical of the diterpenoids labdane, norursane and ent-kaurene, are also observed in the rosemary extract. Therefore, While FTIR provides key information, additional analyses, particularly NMR, are essential for accurate structural identification due to the limitations of FTIR in distinguishing between these diterpenoid classes. This multi-analytical approach enables refined characterization of these fractions, improving understanding of their unique molecular structures.

3.4. Structure elucidation

The fraction F1 was purified as orange-yellow needles. Its molecular formula, $C_{25}H_{36}O_4$, was deduced from UHPLC-MS/MS analysis at *m/z* 399.25 $[M\text{-}H]^-$. The ^1H NMR spectrum (Fig. S1(a)) of **PF1** displayed one singlet methyl group (δ_H 1.20), one doublet of methyl group [δ_H 1.64 (3H, d)], a triplet of methyl groups at δ_H 0.86 (3H, t), seven olefinic protons [(δH 5.32 (1H, m), 5.58 (1H, m), 5.11 (1H, m), 5.48 (1H, m), 5.36 (1H, m), 5.32 (1H, m) and 5.33(m)], two pairs of vinyl protons [δ_H 4.90 (1H, br s), 4.97 (1H, br s), 4.89 (1H, br s) and 4.87 (1H, br s)], and two oxygenated methines [δ_H 4.44 (1H, t) and 4.12 (1H, d)]. The HSQC and HMBC spectra (Fig. S1(b, c)) were considered first to conclude the ^{13}C NMR data, which displayed 25 carbon signals classified as three methyl, six methylenes, and eleven methines [including two oxygenated-bearing carbon at δ_C 80. 32 (C-6) and δ_C 88.6 (C-7), seven olefinic carbons at δ_C 124.5 (C-2), 136.7 (C-3), 124.5 (C-11), 134.0 (C-12), 131.9 (C-13), 128.3 (C-14) and 130.2 (C-3′)], two quaternary carbons (including one olefinic carbons). In addition, one exocyclic methylene group at δ_C 144.8 (C-8), and δ_C 112 (C-16), an ester group at δ_C 172.9 (C-1′) (Table 2). All the positions of the substitutions were deduced using HMBC NMR techniques (Fig. S1(b)). In the HMBC spectrum of **PF1**, the bold blue bonds long-range correlations from 1H to 2 and 1H-3 to C1; 1H-7 to C16; 1H-10 to C1; 1H-11 to C9; 1H-14 to C15; 3H-15 to C8; 1H-16 to C15; 3H-18 to C4, C6 and C10; 1H-C2' to C1' and 1H-4′ to C2' confirmed the labdane diterpenoids skeleton. These data suggested that the structure of PF1 exhibits notable similarities to labdane-type diterpenoids, particularly in its core bicyclic framework and functional group positioning (Chen et al., 2022).

The fraction F5 was purified as a white semi-crystalline substance. Its molecular formula, $C_{28}H_{38}O_3$, was deduced from UHPLC-MS/MS analysis at *m/z* 421.26 $[M\text{-}H]^-$. The ^1H NMR spectrum (Fig. S2(a)) of **PF5** displayed two singlet methyl groups (δ_H 0.64 and 1.32), a doublet of methyl group [δ_H 0.91 (3H, d)], two olefinic protons [(δ_H 5.16 (2H, t) and 5.13 (2H, t)], two pairs of vinyl protons [δ_H 4.56 (1H, br s), 4.69(1H, br s), 4.57 (1H, br s) and 4.67 (1H, br s)] and one oxygenated methine δ_H 3.00 (1H, m). The HMBC and HSQC spectra (Fig. S2(b, c)) were considered first to conclude the ^{13}C NMR data, which displayed 28 carbon signals classified as three methyls, ten methylenes, and seven methines (including one oxygenated carbon at δ_C 77.2 (C-3), two olefinic carbons at δ_C 122.0 (C-12) and 125.08 (C-15) and seven quaternary carbons (four olefinic carbons). In addition, two exocyclic methylene groups at δ_C 110.05 and 150.8 (C-23, C-4), and δ_C 105.1 and 153.4 (C-20, C-30), a carboxylic group at δ_C 177.8 (C-28), and one hydroxylated carbon at δ_C 77.2 (C-3) (Table 2). All the positions of the

Table 2
^{13}C NMR and ^{1}H NMR data of the purified compounds from *R. tournefortii* solid by-product fractionation.

Position	PF1		PF5		PF6	
	δ_C	**δ_H (mult)**	**δ_C**	**δ_H (mult)**	**δ_C**	**δ_H (mult)**
1	24.8	1.94; 1.5 (m)	38.07	1.53; 0.93 (m)	24.2	1.91; 2.08 (m)
2	124.5	5.32 (m)	30.5	1.42; 1.81 (m)	27.4	1.53; 1.45 (m)
3	136.7	5.58 (m)	77.2	3.00 (m)	77.3	3.00 (m)
4	25.1	-	150.8	-	41.2	-
5	56.4	1.92 (m)	54.9	2.16 (m)	55.2	2.16 (m)
6	80.32	4.44 (t)	27.6	1.45; 1.67(m)	38.8	2.11; 1.85 (m)
7	88.6	4.12 (d)	38.9	1. 51; 1.73(m)	125.0	5.13 (t)
8	144.8	-	42.2	-	138.6	-
9	42.5	2.64 (dd)	50.3	1.24 (m)	144.3	-
10	34.8	2.28 (m)	37.1	-	54.9	-
11	124.5	5.11 (m)	24.2	2.17; 1.52 (m)	122.0	5.16 (t)
12	134.0	5.48 (m)	122.0	5.16 (t)	32.2	2.28, 2.15 (m)
13	131.9	5.36 (m)	138.6	-	41.2	2.73 (m)
14	128.3	5.32 (m)	143.3	-	37.09	2.33;1.73 (t)
15	17.1	1.64 (d)	125.08	5.13 (t)	52.8	2.12; 2.10 (s)
16	112	4.90; 4.97 (br s)	34.2	1.8 (m)	153.4	-
17	69.2	4.12; 4.26 (d)	47.4	-	105.2	4.67; 4.57 (br s)
18	24.8	1.20 (s)	52.8	2.10 (d)	64.4	4.01; 4.04 (d)
19	70.2	3.51; 3.5 (d)	37.6	2.32 (m)	18.4	1.56 (s)
20	-	-	153.4	-	178.8	-
21	-	-	32.1	2.15; 2.28 (m)	19.0	1.24 (s)
22	-	-	37.6	1.64; 1.74 (m)	-	-
23	-	-	110.05	4.56; 4.69 (br s)	-	-
24	-	-	-	-	-	-
25	-	-	17.1	0.64 (s)	-	-
26	-	-	23.7	1.32 (s)	-	-
27	-	-	-	-	-	-
28	-	-	177.8	-	-	-
29	-	-	16.5	0.91 (d)	-	-
30	-	-	105.1	4.57; 4.67 (br s)	-	-
1’	172.9	-	-	-	171.9	-
2’	33.8	2.28 (d)	-	-	34.8	2.58 (t)
3’	130.2	5.33 (m)	-	-	22.5	1.24 (m)
4’	113.6	4.89; 4.87 (m)	-	-	14.4	0.86 (overlapped)
5’	-	-	-	-	21.2	1.99 (s)
$\underline{C}H_2CH_3$	62.2	5.19 (m)	-	-	-	-
$CH_2\underline{C}H_3$	14.4	0.86 (t)	-	-	-	-

substitutions were deduced using the HMBC and COSY NMR techniques (Fig. S2(c, d)). In the HMBC spectrum of **PF5**, the bold blue bonds long-range correlations from 1H to 3 to C4; 1H-23 to C3; 3H-25 to C1, C5, C10 and C9; 3H-26 to C9, C7, C8, and C14; 1H-12 to C11 and C18; 3H-29 to C18 and C19; 1H-30 to C19, C20, C21 and C22 confirmed the nor-ursane skeleton. Further, in the 1–1 H COSY spectrum (Fig. S2(d)) of **PF5**, the drown bold green lines range correlations from H-2 to H-3 through OH, H-5 through H-6. H-11 through H-12, H-15 to H-16, H-21 to H-22, H-19 to H-29 were established. These data suggested that the structure of PF5 shares significant similarities with 24-nor-ursane-type triterpenoids (Jang et al., 2005; Wu et al., 2015), particularly in its pentacyclic framework and overall classification within the same family of triterpenoids.

The fraction F6 was purified as a white semi-crystalline substance. Its molecular formula, $C_{26}H_{38}O_5$, was deduced from UHPLC-MS/MS analysis at *m/z* 429.25 $[M\text{-}H]^-$. The ^{1}H NMR spectrum (Fig. S3(a)) of **PF6** displayed three singlet methyl groups (δ_H 1.56, 1.24 and 1.99), two olefinic protons [(δ_H 5.13 (2H, t) and 5.16 (2H, t)], one pair of vinyl protons [δ_H 4.67 (1H, br s) and 4.57(1H, br s)], one oxygenated methine at δ_H 3.00 (1H, m) and one oxygenated-bearing at δ_H 4.01/4.04 (2H, d). The HMBC and HSQC spectra (Fig. S3(b, c)) were considered first to conclude the ^{13}C NMR data, which displayed 26 carbon signals classified as four methyls, nine methylenes (one oxygenated-bearing carbon at δ_C 4.01/4.04 (C-18)), five methines (one oxygenated carbon at δ_C 77.3 (C-3)), two olefinic carbons at δ_C 125.0 (C-7) and 122.0 (C-11) and five quaternary carbons (three olefinic carbons). In addition, one exocyclic methylene groups at δ_C 105.2 (C-17) and 153.4 (C-16), a carboxylic group at δ_C 178.8 (C-20), an ester group at δ_C 171.9 (C-1′) and one hydroxylated carbon at δ_C 77.3 (C-3) (Table 2). Comprehensive analysis of the ^{2}D NMR spectra of **PF6**, especially HMBC, HSQC and 1–1 H COSY (Fig. S3(b, c and d)), allowed the establishment of the structure. In the HMBC spectrum of **PF6**, the bold blue bonds long-range correlations from 1H to 1 to C2; 1H-OH to C2, C3 and C19; 1H-20 to C1 and C5; 1H-6 to C8; 1H-7 to C6; 3H-21 to C9; 1H-11 to C12; 1H-17 to C13 and C14; 3H-19 to C18; 2H-18 to C1’; 1H-2′ to C1’; 1H-2′ to C3’ and 3H-5′ to C4’ confirmed the ent-kaurenes skeleton. Further. in the 1–1 H COSY spectrum (Fig. S3(d)) of **PF6**, the drown bold green lines range correlations from H-2 to H-3 through OH, H-6 through H-7. H-13 through H-14 and H-3′ to H-4′ were established. These data suggested that the structure of PF6 is similar to ent-kaurenes-type diterpenoids (Márquez et al., 2023; Nogueira et al., 2016), particularly in its core bicyclic ring system and classification within the same diterpenoid family.

3.5. Chemical profile of R. tournefortii by-product fractionation

The methanolic extract of *R. tournefortii* solid by-products and its fractions were analyzed using HPLC-DAD, resulting in a detailed phenolic profile highlighting the compound’s complexity and diversity. The reference standards identified included gallic acid, 4-hydroxybenzoic acid, 3-hydroxyflavone, caffeic acid, rosmarinic acid, 2-hydroxycinnamic acid, kaempferol, apigenin, luteolin, carnosol and carnosic acid. These compounds were confirmed by comparing their UV-Vis spectra and retention durations to those of the standards. Additional compounds were identified by referencing the elution scheme for phenolic compounds reported in the literature. On the other hand, some fractions contained compounds that were not detected by HPLC-DAD due to its limitation in analyzing complex molecules or compounds with low UV absorption. To address this limitation and accurately identify these compounds, we utilized the UHPLC-MS/MS method (Table 3), which offers increased sensitivity and specificity. For example, isolated labdane-type diterpenoids and an Asiatic acid isomer were detected in fraction F1, with molecular ion at *m/z* 399.25 and 487.2, respectively. The second fraction also contained labdane-type diterpenoids, along with hinokione, which exhibited a $[M\text{-}H]^-$ ion at *m/z* 293.0. Finally, in the third fraction, hinokione, pyropheophytin-b and hydroxychlorophyll b were described by their $[M\text{-}H]^-$ ion at *m/z* 293.0, 826.4

Table 3
Compounds identified for the first three fractions (F1-F3) by UHPLC-MS/MS.

Identified compounds	Experimental mass $[M\text{-}H]^-$ *m/z*	Fractions	Category	Reference
Labdane-type diterpenoids	399.25	F1, F2	Labdane derivatives	This study
Asiatic acid isomer	487.2	F1	Triterpenoid	(Ibrahim et al., 2022)
Hinokione	293.0	F2, F3	Abietene derivatives	(Linares et al., 2011)
Pyro-pheophytin b	826.40	F3	Chlorophyll derivative	(Ibrahim et al., 2022)
Hydroxy chlorophyll *b*	939.4	F3	Chlorophyll derivative	(Fabrowska et al., 2016)

and 939.4, respectively.

As outlined in Table 4, the chemical profile of the crude extract, represented in Fig. S4(A), is rich in polyphenols, featuring a diverse array of phenolic acids, flavonoids and phenolic diterpenoids. Moreover, examination of the individual fractions revealed valuable insights into the success of the fractionation process and highlighted the distinct chemical characteristics of the isolated compounds. For example, fraction F4 (Fig. S4(a)) exhibited a high content of rosmadial (79.43 %) and carnosic acid (9.70 %), indicating that the elution conditions favoured the isolation of less polar compounds. Similarly, fraction F5 showed a high content of rosmadial (88.2 %) and carnosol (4.7 %) (Fig. S4(b)), confirming the observations made for fraction F4. On the other hand, fraction F6 (Fig. S4(c)) displayed an unusual profile, dominated by diterpene ent-kaurane (36.40 %) and carnosol (47.23 %), suggesting the presence of unique compounds with potential bioactivities, which enabled diterpene ent-kaurane (PF6) to be isolated from this fraction. In addition, fraction F7 (Fig. S4(d)) was enriched in luteolin (70.14 %) and apigenin (19.78 %), demonstrating the effectiveness of the separation techniques for isolating bioactive flavonoids, with luteolin (PF7) subsequently isolated from this fraction, as shown in Fig. S4(d′). Further, fractions F8 and F9 (Fig. S4(e, f)) were found to be rich in hydroxybenzoic acids and 3-hydroxyflavone, respectively. Specifically, fraction F8 was dominated by 4-hydroxybenzoic acid (51.87 %), caffeic acid (27.54 %), and rosmarinic acid (10.27 %), whereas fraction F9 was primarily dominated by 3-hydroxyflavone (40.55 %) and caffeic acid (28.81 %). This distinction constitutes a significant advantage for the present study, as the precise separation of polar phenolic acids highlights the reliability of the method, enabling the targeted extraction of antioxidants to improve the therapeutic efficacy of *R. tournefortii* extracts.

In comparison to our findings, previous studies have conducted detailed investigations into the phenolic compounds present in *R. tournefortii* (Bendif et al., 2017a, 2017b; Boudiar et al., 2018). These studies employed advanced analytical techniques such as high-performance liquid chromatography and mass spectrometry, to characterize bioactive compounds. Importantly, their results align closely with ours identifying major phenolic diterpenes and phenolic acids, including carnosic acid, carnosol, rosmanol, epirosmanol methyl ether, epiisorosmanolethylether, rosmarinic acid, caffeic acid, and gallic acid. Notably, the isolated labdane-type diterpenoids and the ent-kaurane diterpene represent the first identification of these compounds from *R. tournefortii*, underscoring the uniqueness of our findings. Additionally, the detection of flavonoids such as cirsimaritin, hispidulin, apigenin, and luteolin not only supports our findings but also enriches the diversity of the phenolic profile of *R. tournefortii* by-products. It should be noted that, to our knowledge, this study represents the first investigation into the fractionation of *R. tournefortii* by-products. Furthermore, the absence of separate fractions from these by-products suggests that further research is warranted in future studies to fully understand the chemical diversity of this plant.

3.6. Assessment of radical scavenging efficacy

To thoroughly understand the different levels of inhibition observed in the fractions and crude extract, a statistical analysis was performed to determine significant differences in antioxidant capacities across samples (Fig. 3(a, b)). This analysis revealed that the IC50 values for each sample varied significantly, indicating distinct antioxidative capabilities. The analysis identified significant groupings, indicating that the antioxidant potential varies markedly across samples ($p < 0.05$). The crude extract exhibited one of the highest antioxidant activities, while fractions F1 through F4 were statistically grouped with significantly lower antioxidative capabilities (Fig. 3(a)). As fractionation progressed, intermediate to higher antioxidative levels were observed in fractions F5 through F9, reflecting an upward trend in antioxidant potential (Fig. 3 (b)). These statistical distinctions underscore how the concentration and structural characteristics of phenolic compounds within each fraction influence their antioxidative efficacy.

As illustrated in Table 5, the crude extract exhibited the lowest IC50 value (0.04±0.23 mg/mL), indicating the highest antioxidant activity compared to the first fractions (F1–F4), which had significantly higher values. Fractionation progressively enhanced antioxidant activity, as seen from the decreasing IC50 values in fractions F5 to F9, with F7 and F8 showing the best results at 0.35±0.07 mg/mL and 0.36±0.02 mg/mL, respectively. However, the effect of purification on antioxidant activity varied across fractions. For instance, the IC50 of fraction F1 increased slightly from 2.43±0.03 mg/mL to 2.53±0.14 mg/mL after purification, indicating a slight reduction in activity. Similarly, the IC50 of fraction F7 increased from 0.35±0.07 mg/mL to 0.77±0.01 mg/mL post-purification, showing a decrease in antioxidant potential. In contrast, purified F5 showed improved activity with a lower IC50 of 0.76 ±0.009 mg/mL compared to 1.06±0.027 mg/mL in its unpurified form. These results highlight the complex and variable impact of purification, which may remove synergistic molecules or concentrate active

Table 4
Identification of the phenolic compounds of *R. tournefortii* solid by-product fractionation by HPLC-DAD.

Peak number	t_R (min)	Compounds identify	Relative abundance (% of total peak area)							Reference
			Crude extract	F4	F5	F6	F7	F8	F9	
1	2.49	Gallic acid	25.55	-	-	-	-	-	13.2	(Bendif et al., 2017a)
2	3.54	4-Hydroxybenzoic acid	18.77	-	-	-	-	51.87	11.7	(Boudiar et al., 2018)
3	3.98	3-Hydroxyflavone	10.80	-	-	-	-	5.1	40.55	(Boudiar et al., 2018)
4	4.36	Caffeic acid	15.30	-	-	-	-	27.54	28.81	(Ziani et al., 2024a)
5	4.76	Rosmarinic acid	4.02	-	-	-	-	10.27	5.70	(Ziani et al., 2024a)
6	5.31	2-Hydroxycinnamic acid	0.68	-	-	-	-	5.20	-	(Boudiar et al., 2018)
7	6.70	Kaempferol	0.91	-	-	-	2.12	-	-	(Ribeiro-Santos et al., 2015)
8	8.83	Apigenin	0.33	-	-	-	19.78	-	-	(Boudiar et al., 2018)
9	9.68	Hispidulin	0.11	-	-	-	4.02	-	-	(Tzima et al., 2020)
10	12.61	Luteolin	10.95	-	-	-	70.14	-	-	(Ribeiro-Santos et al., 2015)
11	14.21	Cirsimaritin	0.26	-	-	-	3.86	-	-	(Hcini et al., 2021)
12	18.35	Rosmanol	0.13	-	-	3.78	-	-	-	(Linares et al., 2011)
13	19.74	ent-Kaurane diterpene	1.57	-	2.03	36.40	-	-	-	This study
14	19.99	Carnosol	4.21	-	4.7	47.23	-	-	-	(Ziani et al., 2023)
15	21.26	Epirosmanol methyl ether	1.73	-	3.1	2.72	-	-	-	(Romo Vaquero et al., 2013)
16	21.50	Rosmadial	0.90	79.43	88.2	5.25	-	-	-	(Ma et al., 2020)
17	23.69	Epiisorosmanolethylether	0.27	6.78	0.56	2.06	-	-	-	(Ma et al., 2020)
18	25.12	NI	1.81	0.21	1.41	-	-	-	-	(Ziani et al., 2023)
19	27.21	4-Methoxytectochrysin	0.16	3.89	-	-	-	-	-	(Psarrou et al., 2020)
20	29.72	Carnosic acid	0.89	9.70	-	-	-	-	-	(Ziani et al., 2023)

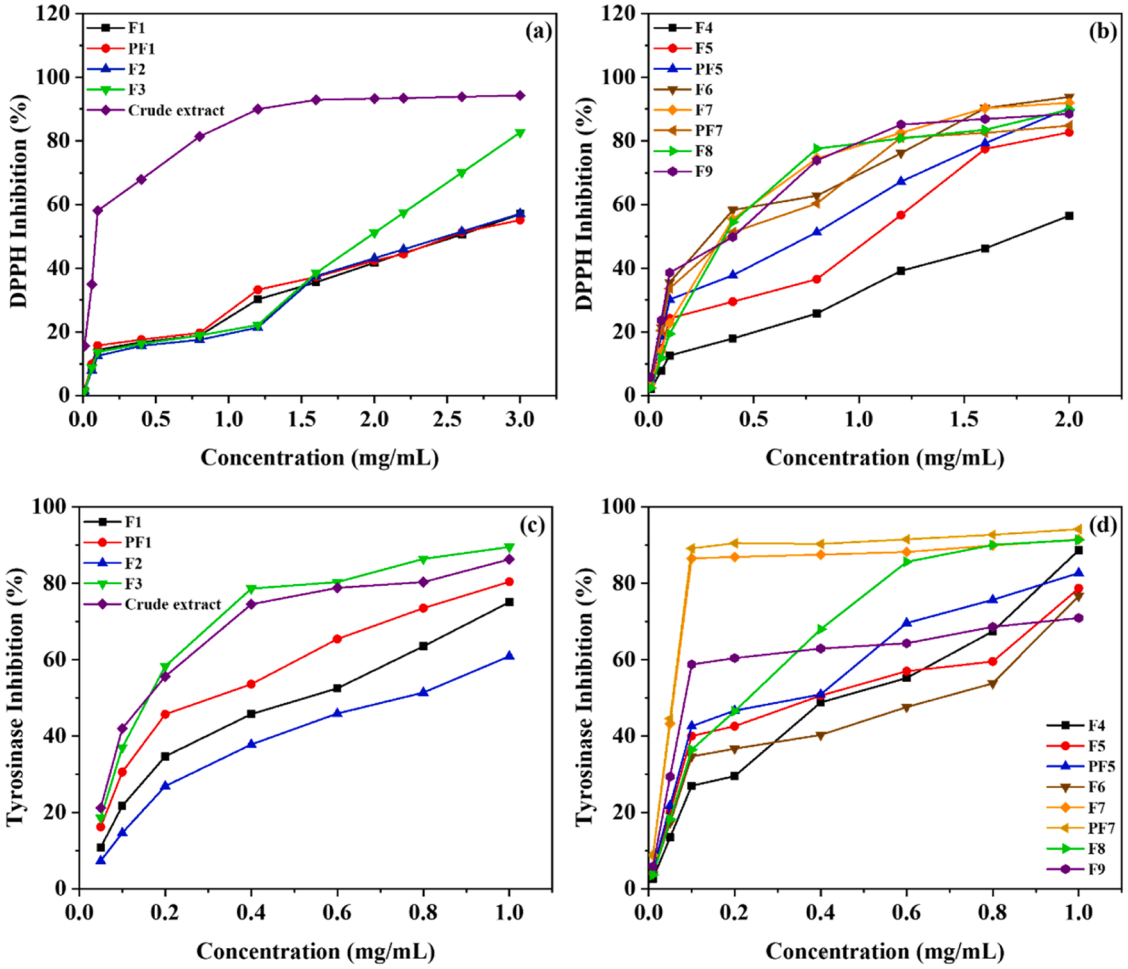

Fig. 3. (a, b) Antioxidant and (c, d) anti-tyrosinase potency of *R. tournefortii* solid by-product fractionation and its purified fraction.

Table 5
IC50 values for the different fractions of *R. tournefortii* solid by-product in the inhibition of DPPH free radicals and tyrosinase.

Samples	Antioxidant and anti-pigmentation performance	
	DPPH IC50 (mg/mL)	**Tyrosinase IC50 (mg/mL)**
Crude extract	0.04 ± 0.23^{a}	0.166 ± 0.009^{a}
F1	2.43 ± 0.03^{d}	0.432 ± 0.033^{c}
PF1	2.53 ± 0.14^{d}	0.272 ± 0.019^{b}
F2	2.39 ± 0.025^{d}	0.684 ± 0.029^{d}
F3	1.96 ± 0.019^{c}	0.157 ± 0.007^{a}
F4	1.81 ± 0.03^{c}	0.368 ± 0.050^{c}
F5	1.06 ± 0.027^{b}	0.312 ± 0.050^{b}
PF5	0.76 ± 0.009^{b}	0.222 ± 0.030^{b}
F6	0.65 ± 0.02^{b}	0.464 ± 0.097^{c}
F7	0.35 ± 0.07^{a}	0.049 ± 0.010^{e}
PF7	0.77 ± 0.01^{b}	0.045 ± 0.007^{e}
F8	0.36 ± 0.02^{a}	0.183 ± 0.015^{a}
F9	0.80 ± 0.003^{b}	0.154 ± 0.039^{a}

*__Note:__ Distinct superscript letters within each column signify that the means differ significantly ($p < 0.05$). Values are presented as Mean ± Standard Deviation ($n = 3$).

compounds depending on the specific fraction. Considering the chemical profiles of the different fractions, fraction F8 had the highest concentration of phenolic acids, known for their strong antioxidant activity due to the presence of multiple hydroxyl groups. This likely explains the high level of inhibition observed in the antioxidant tests. Similarly, fraction F7 contained significant amounts of flavonoids, with luteolin (70.14 %) and apigenin (19.78 %) being the dominant compounds. Flavonoids, such as luteolin, are well-known for their potent antioxidant capabilities, which contribute to free radical inhibition. In contrast, fraction F6 was notable for its high concentration of diterpenoids, including ent-kaurane (36.40 %) and carnosol (47.23 %), with carnosol being particularly effective in neutralizing free radicals.

Compared with the existing literature, our results both align with and differ from existing literature on antioxidant activity patterns. For example, the crude extract showed the highest antioxidant activity, followed by flavonoid-rich fractions, phenolic acids and phenolic diterpenes. This pattern emphasizes synergistic interactions within the crude extract, which is consistent with studies on lingonberry extracts, where crude forms outperform isolated fractions due to molecular interactions (Kostka et al., 2022). Conversely, research on rosemary extracts suggests that fractionation can improve efficacy, particularly for isolated compounds such as carnosic and rosmarinic acids (Karaca et al., 2023; Lefebvre et al., 2021). This corroborates our findings for fractions rich in flavonoids and phenolic acids but also highlights that concentration alone may not achieve the extensive antioxidant effects observed in the full extract.

In summary, while fractionation can enhance antioxidant potency, it can also reduce its effectiveness by eliminating synergistic molecules. Consequently, applications requiring high antioxidant power may benefit from fractions enriched in flavonoids and phenolic acids, while broader antioxidant effects may be better achieved with the crude extract. Further studies should focus on optimized combinations of fractions to balance targeted potency and synergistic benefits, resulting in tailor-made antioxidant profiles for specific applications.

3.7. Evaluation of skin pigmentation control

The anti-pigmentation performance of *R. tournefortii* fractions, assessed by their IC50 values (Table 5) for tyrosinase, shows significant variability, confirmed by statistical analysis. As shown in Fig. 3(c, d), all fractions exhibit significant inhibitory activity at selected concentrations within the range of 0.01–1 mg/mL. Among these, the PF7 and F7 fractions, demonstrate the most potent inhibition, with IC50 values of 0.045 ± 0.007 mg/mL and 0.049 ± 0.010 mg/mL, respectively, which are statistically distinct and significantly lower than all other fractions, indicating their superior tyrosinase inhibition ($p < 0.05$). Other fractions such as F3, F8 and F9 also show strong inhibition with IC50 values in a similar range (e.g. 0.157 ± 0.007 mg/mL for F3), although they are statistically less effective than PF7 and F7. Conversely, fractions such as F1, F2 and F6 show significantly lower inhibition, with IC50 values above 0.4 mg/mL, making them the least effective inhibitors in the group ($p < 0.05$). Interestingly, purification of certain fractions, such as F1 to PF1, significantly improved inhibitory performance, with IC50 values rising from 0.432 ± 0.033 mg/mL to 0.272 ± 0.019 mg/mL ($p < 0.05$), underlining the increased efficacy that can be achieved by purifying fractions.

The purification of the fractions increased their inhibitory activity. For example, fraction F1 exhibited an IC50 of 0.432 ± 0.033 mg/mL, which reduced to 0.272 ± 0.019 mg/mL after purification (PF1), indicating stronger inhibition post-purification. Similarly, fraction F7's IC50 decreased from 0.049 ± 0.010 mg/mL to 0.045 ± 0.007 mg/mL following purification (PF7), reflecting a modest improvement. Both fractions F7 and PF7 are rich in flavonoids, notably luteolin, apigenin and cirsimaritin, compounds known for their potent inhibitory effects. Fraction F3 showed a low IC50 (0.157 ± 0.007 mg/mL), probably due to the presence of chlorophyll derivatives and hinokione, whose specific combination appears to contribute to its inhibitory strength. Furthermore, fractions F8 and F9 had IC50 values of 0.183 ± 0.015 mg/mL and 0.154 ± 0.039 mg/mL, respectively. Despite the lower IC50 of F9, F8 achieved a higher inhibition rate of 91.36 % compared to F9's 70.92 % at a concentration of 1 mg/mL, suggesting that F8's enhanced efficacy may be tied to its unique chemical profile. While F9 primarily comprises 3-hydroxyflavone (40.55 %) and caffeic acid (28.81 %), both recognized for their strong inhibitory properties [40], F8 is mainly composed of 4-hydroxybenzoic acid (51.87 %) and caffeic acid (27.54 %), which may not exhibit the same synergistic effects as the compounds in F9.

Compared with the existing literature, the tyrosinase inhibitory activities observed in *R. tournefortii* fractions strongly align with studies highlighting flavonoids as potent inhibitors. For example, Taslimi (2020) demonstrated that flavonoids exhibit high efficacy with IC50 values as low as 1.64 μM, outperforming standard inhibitors such as kojic acid (IC50 of 9.28 μM). Similarly, our results reveal that flavonoid-rich fractions PF7 and F7 have particularly low IC50 values, reflecting a high affinity for tyrosinase inhibition, confirming the findings of previous studies. In addition, Yener et al. (2020), highlighted flavonoids such as quercetin as superior inhibitors with 405.09 μg kojic acid equivalents per mg, observed comparable high activity in flavonoid-enriched samples. These results concur with those of Morais et al. (2018) who reported that flavonoids generally contribute more significantly to tyrosinase inhibition than chlorophyll derivatives, underlining the role of flavonoids as primary inhibitors. In line with this pattern, our chlorophyll-containing *R. tournefortii* fractions showed weaker inhibition than flavonoid-rich fractions, suggesting a similar mechanism of stable binding to the enzyme's active site.

Furthermore, the variable efficacy observed among *R. tournefortii* fractions with different phenolic acid profiles echoes the findings of Findik et al. (2024) which indicate that certain combinations, such as caffeic and 4-hydroxybenzoic acids, can enhance inhibitory potency through synergistic effects. This suggests that phenolic acids in specific combinations may play a supporting role, although flavonoids remain the main contributors to high levels of inhibition. Overall, these observations indicate that future research should focus on the isolation of specific flavonoid compounds from *R. tournefortii*, particularly those from F7, while also exploring synergies with phenolic acids. Such an approach could optimize inhibitory potency for practical skin-whitening and anti-tanning formulation applications.

3.8. Assessing pathogen-fighting capabilities

The solid by-products of *R. tournefortii* were fractionated using flash chromatography on a silica gel column, yielding several purified fractions. These fractions, together with the crude extract, were then tested for their antimicrobial activity against different pathogenic microbes. Organisms tested included two Gram-negative bacteria *(E. coli* and *P. aeruginosa*), two Gram-positive bacteria (*L. innocua* and *S. aureus*), two molds (*Geotrichum sp.* and *Aspergillus niger*), and two fungi (*Penicillium* and *Rhodotorula glutinis*). Table 6 presents the inhibition diameters, providing a comparative view of the antibacterial activity exhibited by the crude extract and each fraction against these food-borne pathogens. Following purification, statistical analysis ($p < 0.05$) revealed significant differences in inhibition diameters across the tested fractions, underscoring distinct levels of antimicrobial activity for each sample. Fraction PF5 demonstrated the strongest inhibitory activity against several pathogens, including *P. aeruginosa* (15.65 mm), *S. aureus* (17.34 mm), *Aspergillus niger* (16.8 mm), *Penicillium* (16.2 mm), and *Rhodotorula glutinis* (24.1 mm), with results showing statistically significant superiority over other fractions. Similarly, fraction F6 demonstrated significant antimicrobial activity, mostly against *E. coli* (13.85 mm), *L. innocua* (14.95 mm), *Geotrichum sp.* (16.3 mm), and *Rhodotorula glutinis* (24.5 mm).

In contrast, fraction F9 and the crude extract exhibited the lowest inhibitions across all pathogens tested. Meanwhile, other fractions exhibited moderate inhibition levels; for instance, fraction F1 exhibited inhibition values ranging between 10.15 mm and 17.8 mm, while fractions F2 and F3 displayed inhibition zones from 10.1 mm to 21.2 mm. Similarly, fraction F4 provided moderate inhibition against some bacteria (13.35 mm to 16.6 mm) but was limited against certain molds and yeasts. Notably, fraction F5 was particularly effective against some pathogens, including *P. aeruginosa* (14.85 mm), *S. aureus* (16.65 mm), and *Rhodotorula glutinis* (23.3 mm). In addition, fraction F7 showed moderate inhibition (23.7 mm), while its purified form, PF7, exhibited higher activity. In contrast, fraction F8 was inactive against *E. coli* and *P. aeruginosa*, *Aspergillus niger* and *Penicillium*, yet demonstrated notable activity against *S. aureus* (14.25 mm).

Comparing our findings with existing literature highlights the enhanced antimicrobial activity achieved through fractionation, particularly in concentrating specific bioactive compounds within each fraction. For instance, Amaral et al. (2019) found that a fraction of rosemary, rich in carnosic acid, demonstrated superior antibacterial activity, particularly against *S. aureus* and *S. epidermidis*. In our study, fraction F6, which similarly contains carnosol, a diterpenoid with known antimicrobial properties showed strong inhibition against pathogens. This suggests that, as in Amaral et al. (2019) findings, the high concentrations of carnosol in F6 likely enhance its efficacy against various pathogens.

Complementarily, the PF5 in our study reflects the results of Zhong et al. (2021) who reported that the isolation of rosemary fractions rich in triterpenes and other polar compounds had enhanced antimicrobial effects, particularly due to the presence of diterpenes and triterpenoids such as carnosic acid and carnosol. Similarly, PF5 in our study, enriched with 24-nor-ursane triterpenoid compounds, exhibited the highest zones of inhibition, particularly against *P. aeruginosa*, *S. aureus*, and *Rhodotorula glutinis*. According to Wang et al. (2021), these triterpenoids disrupt microbial cell membranes and inhibit critical enzymes, a mechanism that could explain PF5's potent activity. Furthermore, Lax et al. (2012) reported that carnosol exhibits higher antimicrobial potency than carnosic acid, confirming our observations in F6, where the

Table 6
Antimicrobial performance of *R. tournefortii* solid by-product fractionation.

Samples	Inhibition diameter (mm)							
	Bacteria Gram -		**Bacteria Gram -**		**Molds**		**Yeasts**	
	E. coli	***P.aeruginosa***	***L. innocua***	***S. aureus***	***Geotrichum sp.***	***A. niger***	***Penicillium***	***Rhodotorula glutinis***
Ext	8.75±0.35^{b}	10.15±0.21^{b}	9.2±0.14^{b}	9.95±0.35^{b}	11.45±1.20^{b}	-	10.15±0.21^{b}	12.6±0.32^{b}
F1	10.95±0.91^{c}	10.25±0.21^{b}	10.15±0.21^{c}	13.85±0.35^{c}	-	12.5±0.21^{b}	12.5±0.74^{c}	17.8±0.24^{c}
PF1	11.1±0.11 ^{g}	10.5±1.5 ^{f}	12.42±0.23 ^{g}	15.5±0.5 ^{h}	10.7±0.64 ^{f}	12.8±0.25 ^{g}	14.3±0.55^{i}	18.9±0.13^{j}
F2	10.1±0.14^{d}	10.4±0.28^{b}	10.25±0.21^{c}	11.15±0.63^{d}	-	14.4±0.28^{c}	15.4±0.42^{d}	17.3±0.11^{c}
F3	10.95±1.06^{e}	11.65±0.49^{c}	10.85±0.21^{d}	12.15±0.49^{d}	14.95±0.49^{c}	14.6±0.14^{c}	13.2±0.42^{e}	21.2±0.56^{d}
F4	-	13.75±0.77^{d}	13.35±0.25^{e}	16.6±0.14^{e}	-	-	-	14.1±0.22^{e}
F5	13.35±0.21 ^{f}	14.85±0.21^{d}	14.5±0.28 ^{f}	16.65±0.35^{e}	15.85±0.63^{d}	16.65±0.49^{d}	15.9±0.56 ^{f}	23.3±0.13 ^{f}
PF5	14.1±0.55 ^{h}	15.65±0.22 ^{g}	15.23±0.13 ^{h}	17.34±0.32^{i}	15.1±1.2 ^{g}	16.8±0.5 ^{h}	16.2±0.25^{j}	24.1±0.47^{k}
F6	13.85±0.49 ^{f}	14.7±0.28^{d}	14.95±0.21 ^{f}	15.2±0.56 ^{f}	16.3±0.14^{d}	12.4±0.84^{e}	14.3±1.55 ^{g}	24.5±0.52 ^{g}
F7	13.85±0.51 ^{f}	13.35±0.21^{e}	15±0.28 ^{f}	15.5±0.42 ^{f}	12.9±0.56^{e}	14.5±1.27 ^{f}	12.4±0.14 ^{h}	23.7±0.66 ^{h}
PF7	13.9±0.98 ^{h}	14.5±0.91 ^{h}	14.5±0.91 ^{h}	15.95±0.35^{i}	15.6±0.56 ^{g}	15.85±0.49 ^{h}	15.5±0.98^{i}	22.5±0.11 ^{l}
F8	-	-	-	14.25±0.49 ^{g}	10.3±0.31 ^{f}	-	-	11.8±0.22^{i}
F9	-	-	-	-	10.5±0.22 ^{f}	-	-	11.5±0.61^{i}
C^{+}	22.3±0.34^{a}	22.8±0.54^{a}	22.1±0.81^{a}	25.75±0.2^{a}	23.1±0.52^{a}	22.0±1.0^{a}	28.3±1.03^{a}	22.6±0.13^{a}

***Note:** C+; Cycloheximide was used as a positive control for fungi, whereas gentamicin was employed as a control for bacteria. Unique superscript letters in each column indicate a significant difference between the means ($p < 0.05$). Data are shown as Mean ± Standard Deviation, with a sample size of n = 3.

presence of carnosol likely enhances its antimicrobial effect. Overall, these results highlight the potential of specific rosemary fractions, particularly PF5 and F6, as effective natural antimicrobials. Further study of their mechanisms and in vivo efficacy will be valuable in confirming these effects and extending their potential applications as natural preservatives.

3.9. Molecular docking studies

Molecular docking investigations were conducted on the purified compounds PF1, PF5 and PF6 against the alpha-amylase, alpha-glucosidase and tyrosinase enzymes. The high energy values observed for these compounds suggest their stability in the respective active sites. The negative and low docking scores, as summarised in Table 7, indicate strong and favourable binding interactions. Among the compounds, PF5, a 24-nor-ursane triterpenoid, exhibited the most potent inhibition of alpha-amylase, with a docking score of −5.856 kcal/mol, forming stable hydrogen bonds with ASP197 (Fig. 4(A)). This was followed by PF6, an ent-kaurene diterpenoid, which demonstrated a docking score of −5.141 kcal/mol, interacting via hydrogen bonds with LYS200 and GLY306. PF1, a labdane diterpenoid, presented a docking score of −4.886 kcal/mol, forming hydrogen bonds with ASP300 and GLY306. Collectively, all compounds outperformed acarbose, which had a docking score of −4.877 kcal/mol, thus representing more promising candidates for alpha-amylase inhibition. Concerning alpha-glucosidase, PF1 displayed the highest activity, achieving a docking score of −5.898 kcal/mol and forming strong hydrogen bonds with PRO754 and THR764 (Fig. 4(B)). PF6 followed closely, with a docking score of −4.965 kcal/mol, displaying notable inhibition through interactions with GLU169 and ARG585, including hydrogen bonds and a salt bridge. PF5 exhibited similar interactions with MET363 and ARG585 (Fig. 4 **(C)**), registering a docking score of −4.915 kcal/mol. Both PF5 and PF6 exhibited stronger inhibitory activity compared to acarbose (-4.925 kcal/mol), underscoring their efficacy as potential alpha-glucosidase inhibitors. In the context of tyrosinase inhibition, PF5 demonstrated the most significant activity with a docking score of −4.385 kcal/mol, forming hydrogen bonds and salt bridges with ASP275 and LYS281. PF6 followed, scoring −3.435 kcal/mol, while PF1 achieved a score of −2.921 kcal/mol, indicating moderate inhibition. Notably, PF5's performance was comparable to that of kojic acid (-4.888 kcal/mol), pointing to its possible use in the management of hyperpigmentation.

Comparing our findings with existing literature reveals that the docking score of PF5 for alpha-amylase is similar to that of norursane triterpenoids isolated from *Rhododendron brachycarpum*, which exhibit a higher score of −7.9 kcal/mol (Verma et al., 2017). The superior

Table 7
The Docking score and detailed interaction studies of the purified compounds with proteins (1B2Y), (5NN8), and (3NQ1) using SP docking.

Compound Name	Alpha-Amylase			Alpha-Glucosidase			Tyrosinase		
	Docking score (kcal/mol)	**Interacting Amino Acid**	**Type of Interaction Bond**	**Docking score (kcal/mol)**	**Interacting Amino Acid**	**Type of Interaction Bond**	**Docking score (kcal/mol)**	**Interacting Amino Acid**	**Type of Interaction Bond**
PF1	−4.886	GLY306 ASP300	Hydrogen bond Hydrogen bond	−5.898	PRO754 THR764	Hydrogen bond Hydrogen bond	−2.921	GLU274	Hydrogen bond
PF5	−5.856	ASP197	Hydrogen bond	−4.915	MET363 ARG585	Hydrogen bond Salt bridge	−4.385	ASP275 LYS281	Hydrogen bond Salt bridge
PF6	−5.141	LYS200 GLY306	Hydrogen bond Hydrogen bond	−4.965	GLU169 ARG585	Hydrogen bond Salt bridge	−3.435	GLU274 LYS281 LYS281	Hydrogen bond Hydrogen bond Salt bridge
Acarbose	−4.877	ASP197 ASP300 GLY306 GLU240	Hydrogen bond Hydrogen bond Hydrogen bond Hydrogen bond	−4.925	ASP528 ARG600 PHE525 ASP282 ASP616	Hydrogen bond Hydrogen bond Hydrogen bond Hydrogen bond Hydrogen bond	-	-	-
Kojic acid	-	-	-	-	-	-	−4.888	HIS60 GLY216 HIS208	Hydrogen bond Hydrogen bond Pi-Pi stacking

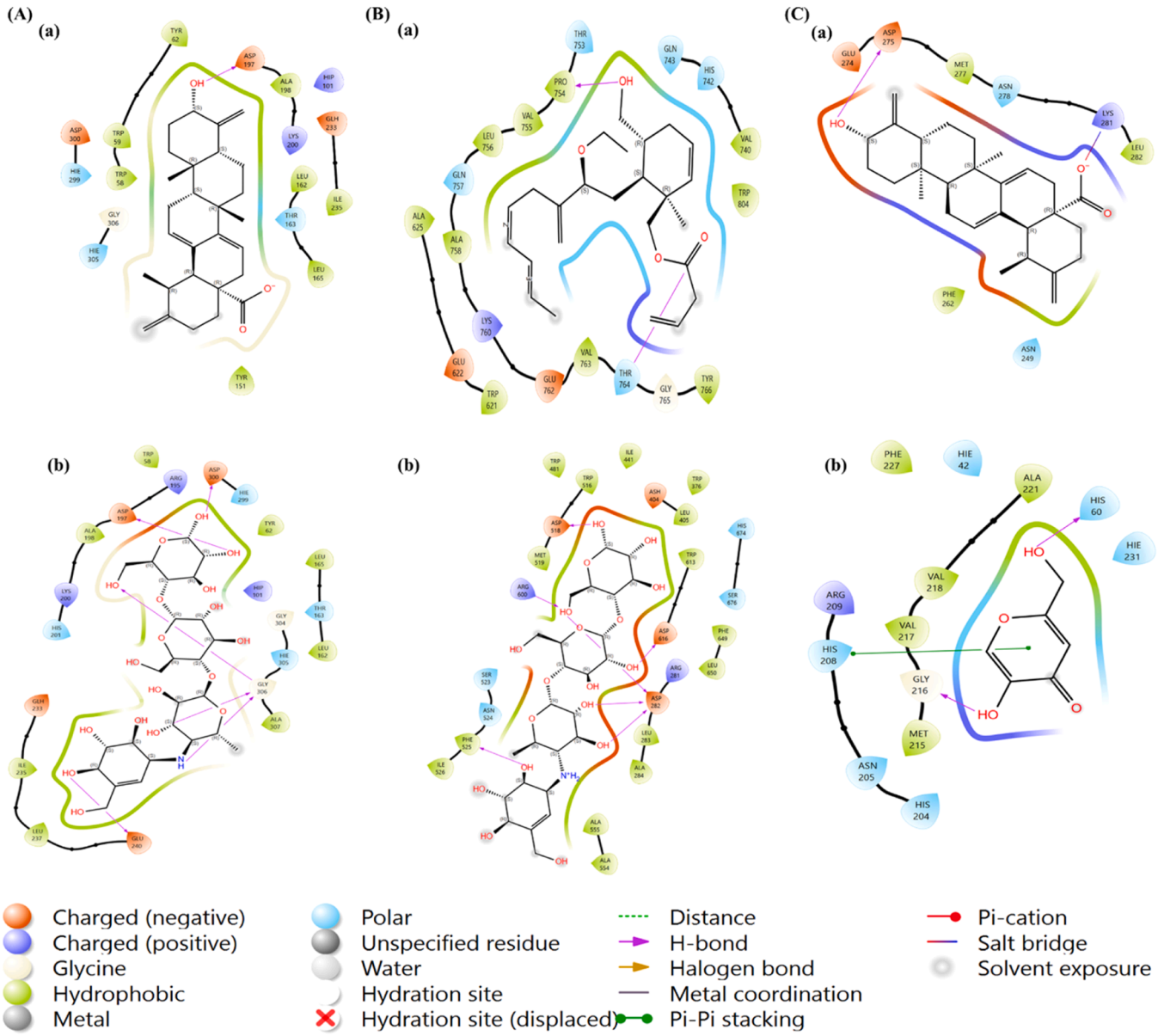

Fig. 4. (A) 2D Intermolecular interactions between (a) PF5 and (b) Acarbose with the active site of α-Amylase (PDB: 1B2Y) protein. (B) 2D Intermolecular interactions between (a) PF1 and (b) Acarbose (Standard) with the active site of α-Glucosidase (PDB: 5NN8) protein. (C) 2D Intermolecular interactions between (a) PF5 and (b) Kojic acid (Standard) with the active site of Tyrosinase (PDB: 3NQ1) protein.

inhibition observed in the reported norursane is attributed to an additional hydroxyl group that enhances hydrogen bonding. In contrast, PF5, despite its olefinic and vinyl protons contributing to hydrophobic interactions, may have reduced flexibility, which affects its hydrogen bonding capability. For alpha-glucosidase, the literature reports that ent-kaurene diterpenoids show stronger inhibition, with docking scores ranging from −9.1 to −9.4 kcal/mol (Hu et al., 2021), compared to the labdane diterpenoid's score of −8.58 kcal/mol (Doorandishan et al., 2024). However, PF1, a labdane diterpenoid, demonstrated stronger inhibition than PF6, an ent-kaurene diterpenoid, emphasizing the importance of functional group arrangement and interaction types in determining inhibitory activity. Regarding tyrosinase, the reported norursane's strong inhibition is reflected in its docking score of −8.5 kcal/mol (Verma et al., 2017). Although PF5 has a lower score, it still exhibits significant activity, though possibly less effective compared to the literature due to the latter's additional hydroxyl group that stabilizes binding. Overall, PF5, PF6, and PF1 exhibit substantial potential as enzyme inhibitors. The observed variability in binding affinities underscores the impact of structural differences in modulating binding interactions. These comparisons indicate that while PF5, PF6, and PF1 show substantial promise as enzyme inhibitors, moving beyond in vitro docking studies to in vivo investigations would provide more definitive evidence of their therapeutic potential. In vivo studies would enable verification of bioavailability, metabolic stability, and inhibitory efficacy in complex biological systems, guiding further optimization for real-world applications in glucose metabolism and pigmentation disorders. Prioritizing in vivo testing could therefore substantiate these findings and inform structural modifications that enhance therapeutic performance.

4. Conclusions

This study highlights the substantial bioactive potential of *R. tournefortii* by-products as promising sources of natural compounds. Thin-layer chromatography successfully separated nine fractions with distinct polarities. Subsequent FTIR, UHPLC-MS/MS, ^{1}D and ^{2}D NMR

analyses confirmed new labdane diterpenoids, nor-ursane triterpenoids and ent-kaurene diterpenoids, adding to the understanding of this plant's unique bioactive profile. In addition, phenolic profiling revealed rosmadial and luteolin as the main phenolic components. Regarding bioactivity, the crude extract exhibited the highest antioxidant activity, demonstrating robust baseline efficacy. However, fractionation enhanced specific bioactivities, with PF7, demonstrating the strongest tyrosinase inhibition. Antimicrobial tests revealed that PF5 effectively inhibited *P. aeruginosa* and *R. glutinis*, while F6 inhibited *E. coli* and *L. innocua*. Molecular docking supported these findings, identifying PF5 as a potent inhibitor of alpha-amylase and tyrosinase, and PF1 as surpassing acarbose in alpha-glucosidase inhibition. These results indicate that while the crude extract excels in antioxidant properties, fractionation and purification amplify specific bioactivities. Collectively, this study highlights the therapeutic and industrial potential of *R. tournefortii* by-products, emphasizing fractionation as a key process for enhancing bioactive properties. Future research should focus on elucidating the mechanisms of action and conducting in vivo assessments to confirm safety and efficacy, unlocking the full potential of these compounds for pharmaceutical, cosmetic, and food preservation applications.

CRediT authorship contribution statement

Abdeslam Asehraou: Visualization, Validation, Methodology. **Ali El Bachiri:** Writing – review & editing, Writing – original draft, Visualization, Validation, Supervision, Conceptualization. **Farooq Sher:** Writing – review & editing, Project administration, Funding acquisition. **Nour Eddine Bentouhami:** Visualization, Methodology, Investigation. **Imane Ziani:** Writing – review & editing, Writing – original draft, Visualization, Methodology, Investigation, Formal analysis, Data curation, Conceptualization. **Hamza Bouakline:** Writing – review & editing, Visualization, Methodology, Investigation. **Mohammed Merzouki:** Validation, Methodology, Investigation, Conceptualization. **Marie-Laure Fauconnier:** Writing – review & editing, Supervision, Resources, Investigation, Formal analysis.

Declaration of Competing Interest

The authors declare that they have no known competing financial interests or personal relationships that could have appeared to influence the work reported in this paper.

Acknowledgements

The authors are highly indebted to Cluster Valbiom Maroc for financial support of the project. The authors acknowledge the financial support from the International Society of Engineering Science and Technology (ISEST) UK.

Appendix A. Supporting information

Supplementary data associated with this article can be found in the online version at doi:10.1016/j.indcrop.2024.120125.

Data availability

Data will be made available on request.

References

Agatonovic-Kustrin, S., Balyklova, K.S., Gegechkori, V., Morton, D.W., 2021. HPTLC and ATR/FTIR characterization of antioxidants in different rosemary extracts. Molecules 26, 6064. https://doi.org/10.3390/molecules26196064.

Amaral, G.P., Mizdal, C.R., Stefanello, S.T., Mendez, A.S.L., Puntel, R.L., de Campos, M. M.A., Soares, F.A.A., Fachinetto, R., 2019. Antibacterial and antioxidant effects of Rosmarinus officinalis L. extract and its fractions. J. Tradit. Complement. Med. 9, 383–392. https://doi.org/10.1016/j.jtcme.2017.10.006.

Bendif, H., Boudjeniba, M., Miara, M.D., Biqiku, L., Bramucci, M., Caprioli, G., Lupidi, G., Quassinti, L., Sagratini, G., Vitali, L.A., 2017a. Rosmarinus eriocalyx: an alternative to Rosmarinus officinalis as a source of antioxidant compounds. Food Chem. 218, 78–88. https://doi.org/10.1016/j.foodchem.2016.09.063.

Bendif, H., Miara, M.D., Kalboussi, Z., Grauzdytė, D., Povilaitis, D., Venskutonis, P.R., Maggi, F., 2018. Supercritical CO2 extraction of Rosmarinus eriocalyx growing in Algeria: chemical composition and antioxidant activity of extracts and their solid plant materials. Ind. Crops Prod. 111, 768–774. https://doi.org/10.1016/j.indcrop.2017.11.056.

Bendif, H., Miara, M.D., Peron, G., Sut, S., Dall'Acqua, S., Flamini, G., Maggi, F., 2017b. NMR, HS-SPME-GC/MS, and HPLC/MS n analyses of phytoconstituents and aroma profile of rosmarinus eriocalyx. Chem. Biodivers. 14, e1700248. https://doi.org/10.1002/cbdv.201700248.

Bensouici, C., Boudiar, T., Kashi, I., Bouhedjar, K., Boumechhour, A., Khatabi, L., Larguet, H., 2020. Chemical characterization, antioxidant, anticholinesterase and alpha-glucosidase potentials of essential oil of Rosmarinus tournefortii de noé. J. Food Meas. Charact. 14, 632–639. https://doi.org/10.1007/s11694-019-00309-y.

Bermúdez-Oria, A., Castejón, M.L., Rubio-Senent, F., Fernández-Prior, Á., Rodríguez-Gutiérrez, G., Fernández-Bolaños, J., 2024. Isolation and structural determination of cis-and trans-p-coumaroyl-secologanoside (comselogoside) from olive oil waste (alperujo). Photoisomerization with ultraviolet irradiation and antioxidant activities. Food Chem. 432, 137233.

Bhattacharjee, B., Jolly, L., Mukherjee, R., Haldar, J., 2022. An easy-to-use antimicrobial hydrogel effectively kills bacteria, fungi, and influenza virus. Biomater. Sci. 10, 2014–2028.

Bouakline, H., Bouknana, S., Merzouki, M., Ziani, I., Challioui, A., Bnouham, M., Tahani, A., El Bachiri, A., 2024. The phenolic content of pistacia lentiscus leaf extract and its antioxidant and antidiabetic properties. Sci. World J., 1998870 https://doi.org/10.1155/2024/1998870.

Boudiar, T., Harfi, B., Segura-carretero, A., 2018. Phytochemical characterization of bioactive compounds composition of Rosmarinus eriocalyx by RP–HPLC–ESI–QTOF–MS. Nat. Prod. Res. 56, 23–65. https://doi.org/10.1111/j.1748-1716.1962.tb02520.x.

Capanoglu, E., Nemli, E., Tomas-Barberan, F., 2022. Novel approaches in the valorization of agricultural wastes and their applications. J. Agric. Food Chem. 70, 6787–6804.

Chen, X., Luo, Q., Hu, W., Chen, J., Zhang, R., 2022. Labdane and isopimarane diterpenoids from Rosmarinus officinalis solid wastes: MS/MS spectrometric fragmentations and neuroprotective effect. Ind. Crops Prod. 177, 114441. https://doi.org/10.1016/j.indcrop.2021.114441.

Doorandishan, M., Pirhadi, S., Gholami, M., Jassbi, A.R., 2024. In silico studies of bis-spiro-and Furano-Labdane diterpenoids from Rydingia persica Scheen (Otostegia persica) as α-glucosidase enzyme inhibitor. Nat. Prod. Res. 1–8.

El Guerraf, A., Jadi, S.Ben, Ziani, I., Dalli, M., Sher, F., Bazzaoui, M., Bazzaoui, E.A., 2023. Multifunctional smart conducting polymers-silver nanocomposites-modified biocellulose fibers for innovative food packaging applications. Ind. Eng. Chem. Res. 62, 4540–4553. https://doi.org/10.1021/acs.iecr.2c01327.

Elyashberg, M., 2015. Identification and structure elucidation by NMR spectroscopy. TrAC - Trends Anal. Chem. 69, 88–97. https://doi.org/10.1016/j.trac.2015.02.014.

Fabrowska, J., Ibañez, E., Łęska, B., Herrero, M., 2016. Supercritical fluid extraction as a tool to valorize underexploited freshwater green algae. Algal Res. 19, 237–245.

Findik, B.T., Yildiz, H., Akdeniz, M., Yener, I., Yilmaz, M.A., Cakir, O., Ertas, A., 2024. Phytochemical profile, enzyme inhibition, antioxidant, and antibacterial activity of Rosa pimpinellifolia L.: a comprehensive study to investigate the bioactivity of different parts (whole fruit, pulp, and seed part) of the fruit. Food Chem., 139921

Freitas, L.C., Barbosa, J.R., da Costa, A.L.C., Bezerra, F.W.F., Pinto, R.H.H., de, Carvalho Junior, R.N., 2021. From waste to sustainable industry: how can agro-industrial wastes help in the development of new products? Resour. Conserv. Recycl. 169, 105466.

Hcini, K., Lozano-Pérez, A.A., Luis Cenis, J., Quílez, M., José Jordán, M., 2021. Extraction and encapsulation of phenolic compounds of tunisian rosemary (Rosmarinus officinalis L.) extracts in silk fibroin nanoparticles. Plants. https://doi.org/10.3390/plants10112312.

Hu, G., Peng, X., Dong, D., Nian, Y., Gao, Y., Wang, X., Hong, D., Qiu, M., 2021. New ent-kaurane diterpenes from the roasted arabica coffee beans and molecular docking to α-glucosidase. Food Chem. 345, 128823.

Ibrahim, N., Abbas, H., El-Sayed, N.S., Gad, H.A., 2022. Rosmarinus officinalis L. hexane extract: phytochemical analysis, nanoencapsulation, and in silico, in vitro, and in vivo anti-photoaging potential evaluation. Sci. Rep. 12, 13102.

Jang, D.S., Kim, J.M., Kim, J.H., Kim, J.S., 2005. 24-nor-ursane type triterpenoids from the stems of Rumex japonicus. Chem. Pharm. Bull. 53, 1594–1596. https://doi.org/10.1248/cpb.53.1594.

Kabubii, Z.N., Mbaria, J.M., Mathiu, P.M., Wanjohi, J.M., Nyaboga, E.N., 2024. Bioassay guided isolation and compounds identification of the anti-diabetic fractions of (rosemary) Rosmarinus officinalis leaves extract. Clin. Phytosci. 10, 16. https://doi.org/10.1186/s40816-024-00378-7.

Karaca, N., Demirci, B., Gavahian, M., Demirci, F., 2023. Enhanced bioactivity of rosemary, sage, lavender, and chamomile essential oils by fractionation, combination, and emulsification. ACS Omega 8, 10941–10953. https://doi.org/10.1021/acsomega.2c07508.

Kostka, T., Ostberg-Potthoff, J.J., Stärke, J., Guigas, C., Matsugo, S., Mirčeski, V., Stojanov, L., Veličkovska, S.K., Winterhalter, P., Esatbeyoglu, T., 2022. Bioactive phenolic compounds from Lingonberry (Vaccinium vitis-idaea L.): extraction, chemical characterization, fractionation and cellular antioxidant activity. Antioxidants 11, 467. https://doi.org/10.3390/antiox11030467.

Lax, V., Rota, M.C., Lora, S., Sotomayor, J.A., 2012. L.) Methanolic Extracts. Relev. Carnosic Acid. Carnosol Rosmarinic Acid. Conc. Vitr. Antioxid. Antimicrob. Act. Rosmarinus o fficinalis.

Lefebvre, T., Destandau, E., Lesellier, E., 2021. Sequential extraction of carnosic acid, rosmarinic acid and pigments (carotenoids and chlorophylls) from Rosemary by online supercritical fluid extraction-supercritical fluid chromatography. J. Chromatogr. A 1639, 461709. https://doi.org/10.1016/j.chroma.2020.461709.

Linares, I.B., Arráez-Román, D., Herrero, M., Ibáñez, E., Segura-Carretero, A., Fernández-Gutiérrez, A., 2011. Comparison of different extraction procedures for the comprehensive characterization of bioactive phenolic compounds in Rosmarinus officinalis by reversed-phase high-performance liquid chromatography with diode array detection coupled to electrospray time. J. Chromatogr. A 1218, 7682–7690.

Liu, T., Sui, X., Zhang, R., Yang, L., Zu, Y., Zhang, L., Zhang, Y., Zhang, Z., 2011. Application of ionic liquids based microwave-assisted simultaneous extraction of carnosic acid, rosmarinic acid and essential oil from Rosmarinus officinalis. J. Chromatogr. A 1218, 8480–8489. https://doi.org/10.1016/j.chroma.2011.09.073.

Ma, Y.-Y., Zhao, D.-G., Zhang, R., He, X., Li, B.Q., Zhang, X.-Z., Wang, Z., Zhang, K., 2020. Identification of bioactive compounds that contribute to the α-glucosidase inhibitory activity of rosemary. Food Funct. 11, 1692–1701.

Mahnashi, M.H., Alqahtani, Y.S., Alqarni, A.O., Alyami, B.A., Jan, M.S., Ayaz, M., Ullah, F., Rashid, U., Sadiq, A., 2021. Crude extract and isolated bioactive compounds from Notholirion thomsonianum (Royale) Stapf as multitargets antidiabetic agents: in-vitro and molecular docking approaches. BMC Complement. Med. Ther. 21, 1–13.

Márquez, A.E., Pérez, A., Rojas, L., Aparicio, R., Ramos, F., Obregón, Y., Usubillaga, A., 2023. A New ent-kaurene diterpenoid isolated from leaves of espeletia semiglobulata cuatrec. and its potential antimicrobial activity. Biol. Med. Nat. Prod. Chem. 12, 151–157. https://doi.org/10.14421/biomedich.2023.121.151-157.

Mir-Cerdà, A., Nunez, O., Granados, M., Sentellas, S., Saurina, J., 2023. An overview of the extraction and characterization of bioactive phenolic compounds from agri-food waste within the framework of circular bioeconomy. TrAC Trends Anal. Chem. 161, 116994.

Mohammadnezhad, P., Valdés, A., Álvarez-Rivera, G., 2023. Bioactivity of food by-products: an updated insight. Curr. Opin. Food Sci. 52, 101065.

Mollica, A., Stefanucci, A., Macedonio, G., Locatelli, M., Luisi, G., Novellino, E., Zengin, G., 2019. Chemical composition and biological activity of Capparis spinosa L. from Lipari Island. South Afr. J. Bot. 120, 135–140. https://doi.org/10.1016/j.sajb.2018.02.397.

Morais, D.V. de, Costa, M.A.P., de, C., Santa Bárbara, M.F., Silva, F., de, L., Moreira, M. M., Delerue-Mato, C., Guimaraes Dias, L.A., Estevinho, M.L.M., Carvalho, C.A.L., de, 2018. Antioxidant, photoprotective and inhibitory activity of tyrosinase in extracts of Dalbergia ecastaphyllum. PLoS One 13, e0207510.

Morlock, G.E., Heil, J., Bardot, V., Lenoir, L., Cotte, C., Dubourdeaux, M., 2021. Effect-directed profiling of 17 different fortified plant extracts by high-performance thin-layer chromatography combined with six planar assays and high-resolution mass spectrometry. Molecules 26, 1468.

Najar, B., Pistelli, L., Cervelli, C., Salvatici, M.C., Fico, G., Giuliani, C., 2020. Volatilome and micromorphological analysis of two rosemary hybrids. Sci. Hortic. 266, 109284. https://doi.org/10.1016/j.scienta.2020.109284.

Nogueira, M.S., Da Costa, F.B., Brun, R., Kaiser, M., Schmidt, T.J., 2016. ent-pimarane and ent-kaurane diterpenes from Aldama discolor (Asteraceae) and their antiprotozoal activity. Molecules 21, 1–14. https://doi.org/10.3390/molecules21091237.

Nunziata, A., De Benedetti, L., Marchioni, I., Cervelli, C., 2019. High throughput measure of diversity in cytoplasmic and nuclear traits for unravelling geographic distribution of rosemary. Ecol. Evol. 9, 3728–3739. https://doi.org/10.1002/ece3.4998.

Peng, Z., Wang, G., Zeng, Q.H., Li, Y., Wu, Y., Liu, H., Wang, J.J., Zhao, Y., 2021. Synthesis, antioxidant and anti-tyrosinase activity of 1,2,4-triazole hydrazones as antibrowning agents. Food Chem. 341, 128265. https://doi.org/10.1016/j.foodchem.2020.128265.

Psarrou, I., Oreopoulou, A., Tsimogiannis, D., Oreopoulou, V., 2020. Extraction kinetics of phenolic antioxidants from the hydro distillation residues of rosemary and effect of pretreatment and extraction parameters. Molecules 25, 4520.

Ribeiro-Santos, R., Carvalho-Costa, D., Cavaleiro, C., Costa, H.S., Albuquerque, T.G., Castilho, M.C., Ramos, F., Melo, N.R., Sanches-Silva, A., 2015. A novel insight on an ancient aromatic plant: The rosemary (Rosmarinus officinalis L.). Trends Food Sci. Technol. 45, 355–368. https://doi.org/10.1016/j.tifs.2015.07.015.

Romo Vaquero, M., Garcia Villalba, R., Larrosa, M., Yáñez-Gascón, M.J., Fromentin, E., Flanagan, J., Roller, M., Tomás-Barberán, F.A., Espín, J.C., García-Conesa, M., 2013. Bioavailability of the major bioactive diterpenoids in a rosemary extract: metabolic profile in the intestine, liver, plasma, and brain of Zucker rats. Mol. Nutr. Food Res. 57, 1834–1846.

Ruan, J.-H., Li, J., Adili, G., Sun, G.-Y., Abuduaini, M., Abdulla, R., Maiwulanjiang, M., Aisa, H.A., 2022. Phenolic compounds and bioactivities from pomegranate (Punica granatum L.) peels. J. Agric. Food Chem. 70, 3678–3686.

Sharma, J., Bhardwaj, V.K., Singh, R., Rajendran, V., Purohit, R., Kumar, S., 2021. An in-silico evaluation of different bioactive molecules of tea for their inhibition potency against non structural protein-15 of SARS-CoV-2. Food Chem. 346, 128933.

Sharma, Y., Velamuri, R., Fagan, J., Schaefer, J., 2020. Full-spectrum analysis of bioactive compounds in rosemary (Rosmarinus officinalis L.) as influenced by different extraction methods. Molecules 25, 4599. https://doi.org/10.3390/molecules25204599.

Shen, N., Liu, Y., Cui, Y., Xin, H., 2022. Large-scale targetedly isolation of biflavonoids with high purity from industrial waste Ginkgo biloba exocarp using two-dimensional chromatography coupled with macroporous adsorption resin enrichment. Ind. Crops Prod. 175, 114264.

Siddique, M.H., Ashraf, A., Hayat, S., Aslam, B., Fakhar-e-Alam, M., Muzammil, S., Atif, M., Shahid, M., Shafeeq, S., Afzal, M., 2022. Antidiabetic and antioxidant potentials of Abelmoschus esculentus: in vitro combined with molecular docking approach. J. Saudi Chem. Soc. 26, 101418.

Sindhu, T., Srinivasan, P., 2015. Exploring the binding properties of agonists interacting with human TGR5 using structural modeling, molecular docking and dynamics simulations. RSC Adv. 5, 14202–14213.

Stefanucci, A., Zengin, G., Llorent-Martinez, E.J., Dimmito, M.P., Della Valle, A., Pieretti, S., Ak, G., Sinan, K.I., Mollica, A., 2020. Viscum album L. homogenizer-assisted and ultrasound-assisted extracts as potential sources of bioactive compounds. J. Food Biochem. 44, e13377. https://doi.org/10.1111/jfbc.13377.

Striegel, A.M., 2020. Method development in interaction polymer chromatography. TrAC Trends Anal. Chem. 130, 115990.

Su, C., Pham, T.T.T., Cheng, H., 2020. Aqueous enzymatic extraction of rosmarinic acid from Salvia officinalis: optimisation using response surface methodology. Phytochem. Anal. 31, 575–582. https://doi.org/10.1002/pca.2922.

Taslimi, P., 2020. Evaluation of in vitro inhibitory effects of some natural compounds on tyrosinase activity and molecular docking study: antimelanogenesis potential. J. Biochem. Mol. Toxicol. 34, e22566. https://doi.org/10.1002/jbt.22566.

Tsiaka, T., Stavropoulou, N.A., Giannakourou, M.C., Strati, I.F., Sinanoglou, V.J., 2023. Optimization of ultrasound-assisted extraction and characterization of the phenolic compounds in rose distillation side streams using spectrophotometric assays and high-throughput analytical techniques. Molecules 28. https://doi.org/10.3390/molecules28217403.

Tzima, K., Brunton, N.P., Rai, D.K., 2020. Evaluation of the impact of chlorophyll removal techniques on polyphenols in rosemary and thyme by-products. J. Food Biochem. 44, e13148.

Vant, J.W., Lahey, S.-L.J., Jana, K., Shekhar, M., Sarkar, D., Munk, B.H., Kleinekathöfer, U., Mittal, S., Rowley, C., Singharoy, A., 2020. Flexible fitting of small molecules into electron microscopy maps using molecular dynamics simulations with neural network potentials. J. Chem. Inf. Model. 60, 2591–2604.

Verma, M., Gupta, S.J., Chaudhary, A., Garg, V.K., 2017. Protein tyrosine phosphatase 1B inhibitors as antidiabetic agents–a brief review. Bioorg. Chem. 70, 267–283.

Wang, S., Zhang, D., Zhu, J., Liu, H., Li, B., Huang, L., 2021. Achyrophenols A–F: polycyclic polyphenol lactone skeletons and a nor-ursane-type triterpenoid from achyrocline satureioides. J. Org. Chem. 86, 12813–12820. https://doi.org/10.1021/acs.joc.1c01447.

Wu, H.R., He, X.F., Jin, X.J., Pan, H., Shi, Z.N., Xu, D.D., Yao, X.J., Zhu, Y., 2015. New nor-ursane type triterpenoids from Gelsemium elegans. Fitoterapia 106, 175–183. https://doi.org/10.1016/j.fitote.2015.09.002.

Yener, I., Kocakaya, S.O., Ertas, A., Erhan, B., Kaplaner, E., Oral, E.V., Yilmaz-Ozden, T., Yilmaz, M.A., Ozturk, M., Kolak, U., 2020. Selective in vitro and in silico enzymes inhibitory activities of phenolic acids and flavonoids of food plants: relations with oxidative stress. Food Chem. 327, 127045. https://doi.org/10.1016/j.foodchem.2020.127045.

Zamuz, S., Munekata, P.E.S., Dzuvor, C.K.O., Zhang, W., Sant'Ana, A.S., Lorenzo, J.M., 2021. The role of phenolic compounds against Listeria monocytogenes in food. A review. Trends Food Sci. Technol. 110, 385–392.

Zhang, W., Chen, Z., Shen, Y., Li, G., Dai, Y., Qi, J., Ma, Y., Yang, S., Wang, Y., 2020. Molecular mechanism and extraction performance evaluation for separation of methanol and n-hexane via ionic liquids as extractant. ACS Sustain. Chem. Eng. 8, 8700–8712. https://doi.org/10.1021/acssuschemeng.0c02234.

Zhang, Y., Greer, R.A., Song, Yuwei, Praveen, H., Song, Yuhua, 2021. In silico identification of available drugs targeting cell surface BiP to disrupt SARS-CoV-2 binding and replication: drug repurposing approach. Eur. J. Pharm. Sci. 160, 105771.

Zhang, Y.-Y., Jiang, H.-Y., Liu, M., Hu, K., Wang, W.-G., Du, X., Li, X.-N., Pu, J.-X., Sun, H.-D., 2017. Bioactive ent-kaurane diterpenoids from Isodon rubescens. Phytochemistry 143, 199–207. https://doi.org/10.1016/j.phytochem.2017.08.009.

Zhong, X.-J., Na, Z., Xin, W., Jin-Jie, L.I., Hui, M.A., Yue, J., Jia-Hui, X.U., Peng-Cheng, L. I.N., Shang, X.-Y., 2022. Three new ursane-type triterpenoids from Rosmarinus officinalis and their biological activities. Chin. J. Nat. Med. 20, 155–160. https://doi.org/10.1016/S1875-5364(21)60103-6.

Zhong, X., Wang, X., Zhou, N., Li, J., Liu, J., Yue, J., Hao, X., Gan, M., Lin, P., Shang, X., 2021. Chemical characterization of the polar antibacterial fraction of the ethanol extract from Rosmarinus officinalis. Food Chem. 344, 128674. https://doi.org/10.1016/j.foodchem.2020.128674.

Ziani, I., Bouakline, H., Bouknana, S., Bentouhami, N.E., Sher, F., Ansar, S., Fauconnier, M.-L., Bnouham, M., El Bachiri, A., 2024a. Sustainable management of rosemary wastewater and essential oil in agri-environmental bioprocessing. Food Biosci. 62, 105263. https://doi.org/10.1016/j.fbio.2024.105263.

Ziani, I., Bouakline, H., Yahyaoui, M.I., Belbachir, Y., Fauconnier, M.-L., Asehraou, A., Tahani, A., Talhaoui, A., El Bachiri, A., 2023. The effect of ethanol/water concentration on phenolic composition, antioxidant, and antimicrobial activities of Rosmarinus tournefortii de Noé hydrodistillation solid residues. J. Food Meas. Charact. 17, 1602–1615. https://doi.org/10.1007/s11694-022-01722-6.

Ziani, I., El Guerraf, A., Bentouhami, N.E., Brahmi, M., Bouakline, H., El Bachiri, A., Fauconnier, M.-L., Ansar, S., Sher, F., 2024b. Nanoreinforcement strategies for enhancing biodegradable composites in biochemical applications within agriwaste valorisation. Biocatal. Agric. Biotechnol. 58, 103223. https://doi.org/10.1016/j.bcab.2024.103223.